The Atmospheric Response to Meridional Shifts of the Gulf Stream SST Front and Its Dependence on Model Resolution

LUCA FAMOOSS PAOLINI,[a,b] PANOS J. ATHANASIADIS,[a] PAOLO RUGGIERI,[a,c] AND ALESSIO BELLUCCI[d]

[a] *Fondazione Centro Euro-Mediterraneo sui Cambiamenti Climatici (CMCC), Bologna, Italy*
[b] *Department of Environmental Science, Informatics and Statistics, Ca' Foscari University, Venice, Italy*
[c] *Department of Physics and Astronomy, University of Bologna, Bologna, Italy*
[d] *Consiglio Nazionale delle Ricerche, Istituto di Scienze dell'Atmosfera e del Clima (CNR-ISAC), Bologna, Italy*

(Manuscript received 7 July 2021, in final form 19 May 2022)

ABSTRACT: The Gulf Stream (GS) plays a key role in shaping the North Atlantic climate. Moreover, the associated sea surface temperature (SST) front undergoes interannual-to-decadal variability that is thought to force significant atmospheric circulation anomalies. However, general circulation models do not accurately reproduce the atmospheric response to SST front variability as estimated from observations. In this work we analyze the atmospheric response to the GS SST front (GSF) shifts in a multimodel ensemble of atmosphere-only simulations forced with observed SSTs (1950–2014). The atmospheric response is found to be resolution dependent. Only the high-resolution simulations produce a wintertime response similar to observed anomalies. More specifically, (i) analysis of the atmospheric thermodynamic balance close to the GSF showed that the anomalous diabatic heating associated to the GSF displacement is mainly balanced by vertical motion and by meridional transient eddy heat transport (not the case for low-resolution models), while (ii) the large-scale response includes a meridional shift of the North Atlantic eddy-driven jet and storm track homodirectional to the GSF displacement. This atmospheric response is accompanied by changes in low-level baroclinicity close to and north of the GSF, resulting from the oceanic forcing and the zonal atmospheric circulation anomalies respectively. The low-level baroclinicity anomalies lead to changes in baroclinic eddy activity and, ultimately, in the jet via eddy–mean flow interaction. Considering the two-way nature of air–sea interactions, using historical atmosphere-only simulations is a powerful way to isolate the impact of realistic oceanic variability on the atmosphere. Our results suggest that interannual-to-decadal predictability may be higher than what low-resolution models currently indicate.

KEYWORDS: Boundary currents; North Atlantic Oscillation; Storm tracks; Air–sea interaction; Surface fluxes; Interannual variability

1. Introduction

The extratropical sea surface temperature (SST) variability on seasonal and interannual time scales has been mainly interpreted as passive oceanic red-noise response to stochastic atmospheric forcing (Frankignoul and Hasselmann 1977). At the same time extratropical SST anomalies have been shown to exert a weak impact on the atmosphere, with the ocean-induced atmospheric response essentially projecting onto intrinsic atmospheric variability modes (Kushnir et al. 2002). However, recent high-resolution observational and numerical studies suggest a more important role for the extratropical ocean regarding its effect on the atmospheric circulation than what was thought before, with impacts extending far beyond the overlying marine atmospheric boundary layer (MABL). This is true for western boundary current (WBC) areas, where a large portion of the SST variability is driven by intrinsic oceanic processes (Vivier et al. 2002; Dong and Kelly 2004; Deser et al. 2010; Smirnov et al. 2014; Bellucci et al. 2021). Furthermore, these regions are characterized by very strong SST gradients (oceanic fronts), determining important features of the climate system. Observations and numerical analyses have shown that oceanic frontal areas are associated with upward motion extending all the way up to the upper troposphere. The resulting upper-tropospheric divergence acts as an important source of stationary Rossby waves that produce responses in remote areas downstream (Minobe et al. 2008). The presence of the SST front has been shown to be also relevant in shaping zones of intense baroclinic eddy activity and consequently determining the North Atlantic storm track and eddy-driven jet (Hoskins and Valdes 1990; Brayshaw et al. 2011). Nakamura et al. (2004) argued that it is the differential diabatic heating supplied across oceanic fronts that maintains low-level baroclinicity necessary for baroclinic instability growth, with sensible heating playing the most important role (Hotta and Nakamura 2011). In addition, in relation to the above-mentioned vertical motion, SST fronts anchor a narrow band of precipitation because of the atmospheric pressure adjustment to SST differences across oceanic fronts and low-level wind convergence in the MABL at the warm side of the SST front (Pan

Denotes content that is immediately available upon publication as open access.

Supplemental information related to this paper is available at the Journals Online website: https://doi.org/10.1175/JCLI-D-21-0530.s1.

Corresponding author: Luca Famooss Paolini, luca.famooss@cmcc.it

DOI: 10.1175/JCLI-D-21-0530.1

et al. 2002; Minobe et al. 2008). As a result of intrinsic oceanic variability and atmospheric forcing, frontal regions undergo broad meridional shifts and varying meandering, with distinct impacts on the atmospheric circulation (Joyce et al. 2009; Sato et al. 2014; O'Reilly and Czaja 2015). For example, Nakamura and Yamane (2009) showed that positive small-scale SST anomalies along the Gulf Stream (GS), associated with its poleward shift and/or the enhancement of its heat transport, may be responsible for the intensification of low-level baroclinicity in larger portions of the North Atlantic. These anomalies intensify the baroclinic activity along the North Atlantic storm track, with a consistent poleward displacement of the eddy-driven jet stream. Another example is the study of O'Reilly and Czaja (2015), in which they compared the atmospheric state during periods of intense and elongated Kuroshio Extension SST front with the one during periods of relatively weak and convoluted front. They observed that the periods of stronger SST front are associated with an intensified low-level baroclinicity and consistently an increased eddy heat transport in the western Pacific. Then, an anomalous barotropic flow is forced in the eastern Pacific via eddy–mean flow interaction, with a greater occurrence of blocked days. All these aspects highlight that part of atmospheric variability in the extratropics could be linked to the variability of limited oceanic areas (WBCs), with the latter acting as a source of atmospheric predictability, especially on interannual and decadal time scale (Joyce et al. 2019; Athanasiadis et al. 2020).

Despite these advancements, the dynamics underpinning the local atmospheric response to oceanic front variability are not fully understood, while the associated large-scale response is not yet well established. Even if state-of-the-art atmospheric models with horizontal resolutions close to the oceanic deformation radius (~50 km) are more reliable than previous models and better represent the observed climate, important intermodel discrepancies continue to emerge (Czaja et al. 2019). Smirnov et al. (2015) have shown that in an atmospheric general circulation model (AGCM) with horizontal resolution of 1° the atmospheric response to shifts in the Oyashio Extension SST front is weak and exhibits features generally consistent with the paradigm of a steady linear response to a near-surface heat source (Hoskins and Karoly 1981). Instead, in the AGCM with horizontal resolution of 0.25° the near-surface circulation is substantially weaker, while the vertical motion is stronger and deeper (affecting the upper troposphere) and the surface meridional eddy heat transport largely balances the SST-induced diabatic heating anomalies. The differences in vertical motion between these two AGCMs recall results from Feliks et al. (2004). Using a very idealized framework, they showed that a narrow oceanic front is able to force the atmospheric circulation above the MABL through thermal pumping of vertical velocity. However, since oceanic fronts have a width of 100 km or less, only sufficiently high-resolution models can represent this mechanism. In line with this, Nakamura and Yamane (2009) argued that only models with a grid spacing no larger than 50 km are able to adequately resolve slight meridional shift of the GS and its impact on the large-scale atmospheric circulation. Ma et al. (2017) showed that a Weather Research and Forecasting (WRF) Model with a 27-km resolution is much more sensitive to mesoscale SST anomalies along the Kuroshio Extension compared to the model with a 162-km resolution. The high-resolution model version exhibits a southward shift of the eastern North Pacific storm track and jet stream when the mesoscale SST anomalies are smoothed; in contrast, the low-resolution model is not able to resolve the small-scale diabatic processes associated with the mesoscale SST forcing and therefore shows a weak response in eddy activity and large-scale circulation for the same smoothing in oceanic boundary conditions. Looking at single atmospheric instabilities, Willison et al. (2013) have shown that a WRF Model with a 20-km horizontal resolution exhibits enhanced frontal dynamics in North Atlantic midlatitude cyclones compared to the same WRF Model with a 120-km resolution. The authors highlighted a more intense positive feedback between cyclone intensity and latent heat release in the high-resolution model, resulting in the intensification of the storm track as well as in the strengthening of the jet stream. Following these results, Sheldon et al. (2017) argued that the diabatic heating in the warm conveyor belt of cyclones traveling close to the GS SST front (GSF) is directly proportional to the number of air-parcel trajectories feeding the upward motion.

Despite these efforts, the number of studies dealing with the impact of horizontal resolution on the atmospheric response to oceanic forcing is still limited. In addition, previous analyses are based on idealized experimental frameworks forcing the atmosphere with fixed and unrealistic SST anomalies. Finally, such past studies have been limited to single-model assessments. A multimodel analysis to systematically investigate differences between the low-resolution and high-resolution atmospheric response to realistic SST variability linked to the meridional shifts of the GSF is still lacking.

Moreover, the very character of the actual large-scale atmospheric response to such oceanic variability is not well established. Most recently, Joyce et al. (2009 2019), using observational data, presented evidence for significant meridional shifts in the North Atlantic eddy-driven jet and storm track as a homodirectional response to the GSF shifts, including dynamically consistent changes in the distribution of blocking frequency. Such an important response has been elusive to detect in the past (Joyce et al. 2000; Frankignoul et al. 2001) and it still remains to be better understood dynamically, isolated from the actual coupled variability framework in which it occurs.

The objective of this study is twofold: on the one hand it aims at assessing the dependence of the local atmospheric response to the GSF shifts on model resolution, in particular the atmospheric horizontal resolution, and on the other it aims at providing further evidence on the character of the large-scale atmospheric response by assessing the latter in isolation from the coupled variability in which is embedded, using atmosphere-only simulations. The atmospheric response has been investigated in the context of the High Resolution Model Intercomparison Project (HighResMIP), by analyzing historical simulations performed with three AGCMs, each run at two different horizontal resolutions. The AGCMs have been forced with the same observed SSTs. Understanding the impact of horizontal resolution on air–sea interaction can

TABLE 1. HighResMIP models. Columns detail the institution name, the model name, the nominal resolution, the number of vertical levels, the number of members used for analysis, and the model reference.

Institution	Model	Nominal resolution (km)	Vertical levels	Members	Reference
EC-Earth-Consortium	EC-Earth3P	100	91	3	Haarsma et al. (2020)
	EC-Earth3P-HR	50	91	3	
Met Office Hadley Centre (MOHC)	HadGEM3-GC31-MM	100	85	3	Roberts et al. (2018)
	HadGEM3-GC31-HM	50	85	3	
ECMWF	ECMWF-IFS-LR	50	91	8	Roberts et al. (2019)
	ECMWF-IFS-HR	25	91	6	

shed light on the influence of extratropical oceanic variability on the atmosphere, with important implications for climate predictions and climate change studies.

The manuscript is structured as follows. In section 2 the HighResMIP dataset, the SST anomalies associated with the GSF shifts, and the methodological approach are described. In section 3 the atmospheric response to the GSF shifts is presented. In section 4 we present a heat budget analysis along, across, and above the GSF as well as in the North Atlantic basin, in order to investigate ways that diabatic heating is balanced locally and at a wider scale. In section 5 we discuss some large-scale features of the atmospheric response to the GSF shifts. Finally, in section 6 we summarize the results, highlighting the most salient outcomes of the present work.

2. Data and methodological approach

a. Data

The HighResMIP is part of the wider phase 6 of the Coupled Model Intercomparison Project (CMIP6), and it was designed with the specific objective of investigating the impact of increasing model horizontal resolution on the representation of the observed climate and of an array of important physical processes (Haarsma et al. 2016). As such, it provides an ideal framework for a multimodel analysis of the impact of increasing model resolution on the atmospheric response to oceanic forcing. In this study, an ensemble of six atmosphere-only historical simulations have been analyzed. Three different models have been used, each run with two configurations differing only in their horizontal resolution. Hereafter we will refer to model configurations with a nominal resolution coarser than 50 km as R100 models, and those with a nominal resolution finer than or equal to 50 km as R50+ models. Each model has been forced with the HadISST2 sea ice concentration and SST dataset, provided at daily frequency in the period 1950–2014 on a 0.25° grid (Kennedy et al. 2017). For each model a multimember ensemble of simulations has been used, and the results in the following sections refer to the respective ensemble means. This specific experimental design and the use of multimember ensembles allows a more robust identification of the atmospheric response forced by the observed oceanic variability as the ensemble averaging aids the forced response to emerge from the chaotic atmospheric variability, which is particularly strong at midlatitudes. The models considered in this study are EC-Earth3P (Haarsma et al. 2020), ECMWF-IFS (Roberts et al. 2018), and HadGEM3-GC31 (Roberts et al. 2019). Table 1 shows the respective model configurations, nominal resolutions (km), number of vertical levels, number of members, and reference (model documentation). Additional details about the experimental setup can be found in Haarsma et al. (2016; see "Tier 1–highresSST-present" experiment). Finally, model results have been compared to ERA5 reanalysis (Hersbach et al. 2020), here used as a surrogate of observations in the period 1950–2014.

b. Gulf Stream sea surface temperature front shift

In this study, the atmospheric response to interannual GSF meridional shifts in the winter season (December–February) has been investigated. Previous studies have shown that the north–south shift of GSF represents the leading variability mode of SST variability in the GSF area on interannual and longer time scales (Joyce et al. 2009; Kwon and Joyce 2013). The winter season has been selected because this is the time of the year characterized by the most intense heat exchanges between ocean and atmosphere, resulting in a stronger impact of the ocean variability on the atmosphere (Kallberg et al. 2005). The GSF has been defined as the line of maximum SST gradient. The SST gradient magnitude has been calculated for winter mean SST fields, smoothed with a 2D spatial Gaussian kernel filter applied to a 7×7 grid point box, with standard deviation equal to 2. The smoothing has been applied in order to remove isolated points of strong SST gradient not representative of the GSF position. The latitude of the GSF has been averaged in the 50°–68°W longitudinal range, where the GS is more zonally oriented. Then, this zonally averaged latitude of the GSF has been used to define the "North" and "South" phases of the front shift via the respective upper and lower tercile categories. Figure 1 shows the SST composites obtained by averaging all years over the upper and below the lower terciles (i.e., the "North" and "South" phases of the GSF), consisting of 22 and 21 years, respectively. The resulting SST pattern shows a tripolar structure extending to the entire North Atlantic in both GSF phases but of opposite sign (Fig. 1). The "North" ("South") phase is associated dominantly with positive (negative) anomalies along the climatological position of the GSF in winter, as well as in the midlatitude North Atlantic to the south of the GSF and the North Atlantic Current, and negative (positive) anomalies

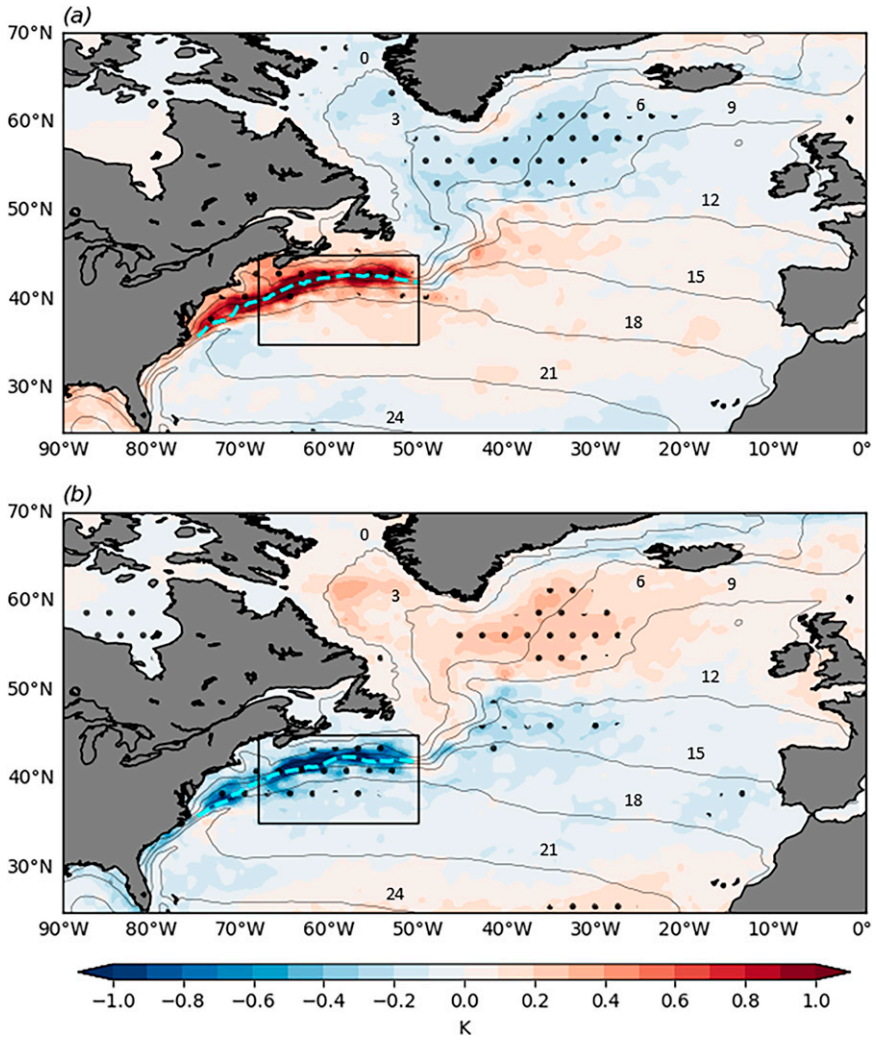

FIG. 1. SST (K; color shading) anomalies associated to (a) "North" and (b) "South" phases of the GSF in winter (DJF) in the HadISST2 dataset. The "North" ("South") phase has been defined as the upper (lower) tercile of GSF mean latitude. The respective climatological position of the SST front is indicated by the cyan dashed line. The black contours indicate winter SST climatology. The black rectangular frames indicate the longitudinal range over which the GSF mean latitude and subsequent diagnostics (Figs. 8 and 9; see also Fig. S2) have been calculated. Black dots denote anomalies that were found to be statistically significant at the 90% confidence level (details in section 2).

farther north in the subpolar gyre region and south of 30°N. The anomalies are strongest close to the GSF with values exceeding 1 K (absolute departures). In the remaining part of the basin, the SST anomalies are much weaker and lower than 0.4 K. The corresponding SST anomalies in other parts of the global ocean have been assessed, and their significance in remotely forcing an atmospheric circulation response over the extratropical North Atlantic is discussed in the following.

In Fig. 2 the GSF latitude time series in the period 1950–2014 is presented. The years corresponding to the "North" ("South") phase are highlighted with red (blue) stars. The index features an interannual variability component associated with SST front latitudinal shift of about 0.2°–0.5°. A lower frequency, decadal-scale component is also evident associated with weaker amplitude meridional displacements. The North Atlantic SST variability described above has been previously interpreted as the oceanic response to North Atlantic Oscillation (NAO) forcing via SHF and Ekman currents, explaining an important portion of the extratropical SST variability on seasonal and interannual time scale (Cayan 1992; Deser et al. 2010). However, it has been shown that close to the GSF the SST variability is primarily driven by oceanic processes, such as oceanic heat transport and diffusion, with the former admittedly remaining subject to the atmospheric forcing (Kelly and Qiu 1995; Dong and Kelly 2004; Kelly et al. 2010; Kwon et al. 2010; Minobe et al. 2010;

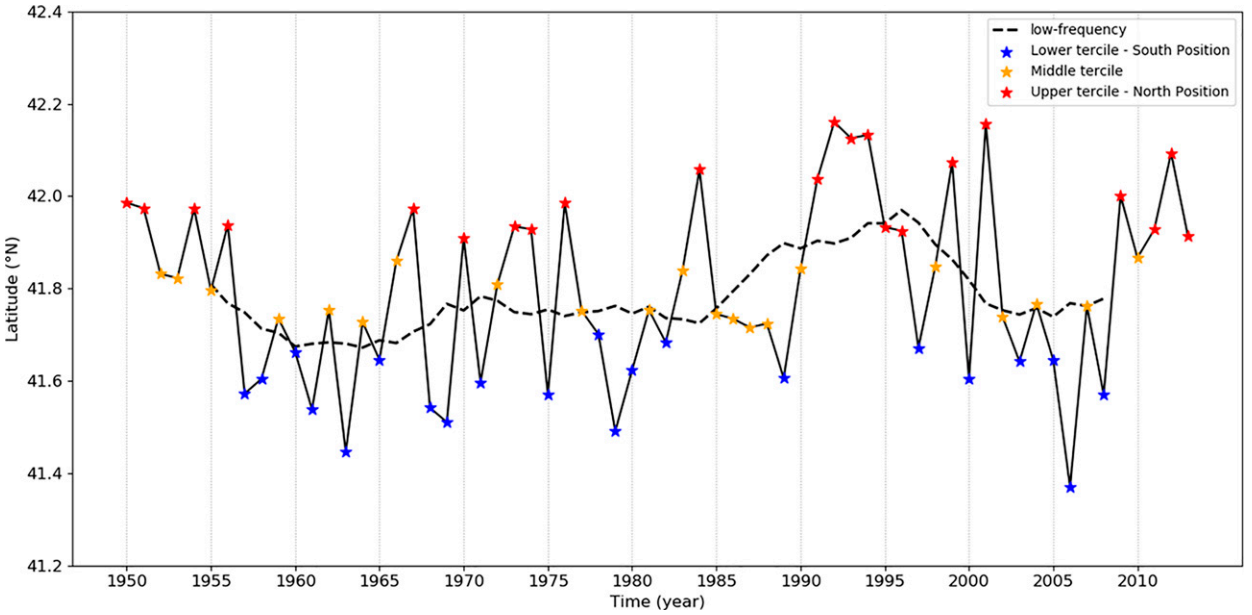

FIG. 2. Winter-mean latitude of the GSF averaged in the 50°–68°W longitudinal range. Red, yellow, and blue stars represent years in which the GSF latitude falls, respectively, in the upper, middle, and lower tercile categories (i.e., North, Middle, and South position). The dashed line is the 10-yr running mean applied to GSF latitude time series.

Patrizio and Thompson 2021). Therefore, the SST anomalies described here are the surface oceanic signature of both historical atmospheric forcing and intrinsic oceanic variability. This aspect must be taken into account to avoid erroneous considerations during the analysis of data, especially observations. A number of studies (e.g., Czaja and Frankignoul 2002; Ciasto and Thompson 2004; Wills et al. 2016) present evidence that SST anomalies in the vicinity of the GS may affect the large-scale atmospheric circulation up to several months ahead. Some authors have argued that meridional shifts of the GSF may be key in explaining decadal NAO variability and predictability (Feliks et al. 2011; Joyce et al. 2019; Athanasiadis et al. 2020).

c. *Methods*

The atmospheric circulation anomalies associated with the GSF shifts have been analyzed using composites of the "North" minus "South" phase of the GSF. For assessing the statistical significance of the differences between the two GSF phases, a two-sided Student's *t* test against the null hypothesis of no difference has been applied at the 90% significance level. Specifically, the impact of the GSF meridional displacement on the atmospheric circulation has been characterized through the analysis of monthly near-surface winds, mean sea level pressure (SLP), surface heat fluxes (SHF; i.e., the sum of turbulent sensible and latent heat fluxes), zonal winds at 850 hPa (U850; representing the eddy-driven jet), the meridional temperature gradient (related to baroclinicity) at 925 hPa, and, starting from daily data, the 2–6-day high-pass meridional eddy heat flux (MEHF) at 850 hPa and blocking frequency. The eddy-driven jet response has been analyzed both in terms of the associated anomalous field and jet latitude variability. As in Woollings et al. (2010), the daily zonal winds at 850 hPa have been zonally averaged in the 0°–60°W longitudinal range, masking out Greenland and the Atlas Mountains that intersect the 850-hPa isobaric surface. Then a 10-day low-pass Lanczos filter with a window of 61 days (Duchon 1979) has been applied to the resulting fields. The jet stream latitude has been defined as the latitude of maximum westerly wind speed in the 15°–75°N latitudinal range. To detect atmospheric blocking, the 2D large-scale blocking index defined in Davini et al. (2012) has been adopted including the condition to avoid the detection of false blocking events at low latitudes (Athanasiadis et al. 2014). In addition to the above mentioned diagnostics, the monthly zonal-mean circulation and the atmospheric heat budget in the vertical–meridional cross section in the 50°–68°W longitude range have been computed.

d. *SST front-following coordinate system*

For analyses in the vertical–meridional cross section an SST front-following coordinate system has been devised. To define the SST-front coordinate system, the position of the GSF computed on the original HadISST2 0.25° grid has been assigned to the nearest grid point of the native grid of each AGCM. Since the oceanic grid is finer than those of AGCMs, the GSF position in each model is slightly different from the original one. However, this choice has no significant effect on atmospheric diagnostics calculated along the vertical–meridional plane because the AGCMs would not have been affected by subgrid SST front features anyway. Starting from the interpolated GSF position, a 3D space has been considered with the abscissa representing the displacement along the GSF, the second horizontal axis representing the

meridional direction, and the vertical axis representing pressure levels. Then, the vertical–meridional plane has been derived averaging the diagnostics in the alongfront direction. The zonal average has been taken avoiding grid points over land north of the GSF. The SST front-following coordinate system has allowed for taking into account the poleward tilt of the SST front and carrying out the analysis purely along the cross-front direction.

3. Atmospheric response to Gulf Stream SST front shift

Figure 3 shows near-surface wind, SLP, and SHF composite differences on the GSF meridional displacement in the models and the observations. R100 models exhibit a low pressure anomaly downstream of the GSF that is largely consistent with meridional temperature advection in the area along the GSF tending to balance the anomalous diabatic heating. The general features of the atmospheric response in R100 models recall what one would expect at the surface for an extratropical shallow heat source in theoretical linear models (Hoskins and Karoly 1981). On the other hand, R50+ models show a high pressure anomaly downstream of SST anomalies, with winds blowing from the southern portion of North Atlantic poleward in the vicinity of the SST front. This is in contrast to what is expected from the linear theory. The R50+ response resembles results from other studies, showing that the atmospheric response is strongly mediated by transient eddy fluxes balancing the anomalous diabatic heating (Peng et al. 1997; Peng and Whitaker 1999; Watanabe and Kimoto 2000). It is specified that in R50+ models the SLP anomalies are statistically significant over a large part of the North Atlantic at the 90% confidence level. This is not the case for R100 models, for which the statistically significant anomalies over the same region are more limited.

SHF anomalies are particularly intense close to the GSF both in R100 and R50+ models, reaching values that correspond to an important portion of winter climatology (about 15%–20%). These largely coincide with the area of strongest alongfront SST anomalies. For R100 models meridional temperature advection tends to balance this anomalous diabatic heating associated with the GSF shifts. Indeed, the anomalous atmospheric circulation transports cold air from higher latitudes toward the GSF area. In contrast, in R50+ models meridional temperature advection does not tend to balance the anomalous diabatic heating but to exacerbate the induced temperature tendencies. This is consistent with the northward advection of warm air from lower latitudes. This fact indicates that other processes, different from horizontal temperature advection, have a key role in balancing heating anomalies above the GSF. This aspect will be discussed in more detail in section 4. Unlike in the frontal area, SHF differ in other portions of the ocean basin. R100 models show a negative SHF south of Greenland and on the southern flank of the GSF and positive ones in the central North Atlantic. In contrast R50+ models develop positive fluxes south of Greenland and on the eastern North Atlantic, with negative values mainly confined at the southern flank of the GSF. For the ECMWF model with a nominal resolution of 50 km (Fig. 3f) and the Met Office Hadley Centre (MOHC) R50+ model (Fig. 3e) the negative SHF anomalies extend more northward compared to the other two R50+ models, reaching the southern Greenland coast. These discrepancies are consistent with near-surface wind differences among R50+ models. In Figs. 3c and 3g, positive SHF close to the Greenland coast are associated with surface wind blowing from inland of North America and then transporting cold and dry continental air that is warmed by the ocean. In Figs. 3e and 3f, negative SHF close to Greenland are associated with near-surface wind blowing from the southern North Atlantic and then transporting warm and wet air that reduces the thermal air–sea contrast. Apart from these discrepancies, R50+ models are more comparable to each other than R100 ones. Furthermore, R50+ models reproduce general features of surface atmospheric anomalies found in the ERA5 dataset. As depicted in Fig. 3a, observations show a zonally elongated anticyclonic circulation anomaly in surface winds, consistent with the positive SLP anomaly downstream from the heating source (statistically significant at 90% confidence level). SHF anomalies are positive in the northern flank of the GSF and negative in its southern flank as the respective wind anomalies suggest in an area of climatological westerly surface flow. Consequently, the SHF anomalies are spatially anticorrelated with the SST anomalies as expected for atmospheric forcing to the ocean. This implies that the large-scale SST anomalies seen in Fig. 1 away from the GSF are the fingerprint of local atmospheric forcing that occurred in the real system during and prior to the GSF shifts.

The SHF, SLP, and SST patterns in observations recall positive (minus negative) NAO-like forcing on the ocean. This is in line with previous studies showing that the GS meridional shifts are correlated with the low-frequency NAO variability at a positive lag of about 1–2 years with the ocean following the atmospheric forcing (Taylor and Stephens 1998; Frankignoul et al. 2001; Sanchez-Franks et al. 2016). However, the comparison between AGCMs and observations suggests that, as soon as the GSF shift is established, the ocean provides a positive feedback on the atmospheric circulation, and that the realistic representation of this feedback in AGCMs requires a sufficiently high horizontal resolution (as R100 models fail to reproduce it).

In Fig. 4 zonal wind anomalies at 850 hPa are presented. R100 models generate a southward shift of the eddy-driven jet, with negative anomalies to the north of the climatological jet position and positive anomalies to the south, even though significant differences can also be seen between the two models. In contrast, R50+ models exhibit anomalies of the opposite sign, indicating a northward shift of the jet. These anomalies recall the pattern seen in the observations (ERA5), yet with a lower amplitude. Then, for both the R100 and the R50+ models, similar but stronger zonal wind anomalies were found aloft (not shown) indicating an equivalent barotropic structure extending throughout the troposphere.

To assess in more detail the response of the North Atlantic eddy-driven jet to the GSF shifts, the jet latitude distributions (PDFs) for each phase of the GSF position are shown for each model in Fig. 5. As specified in section 2, it is recalled that the jet stream latitude has been defined through the zonal

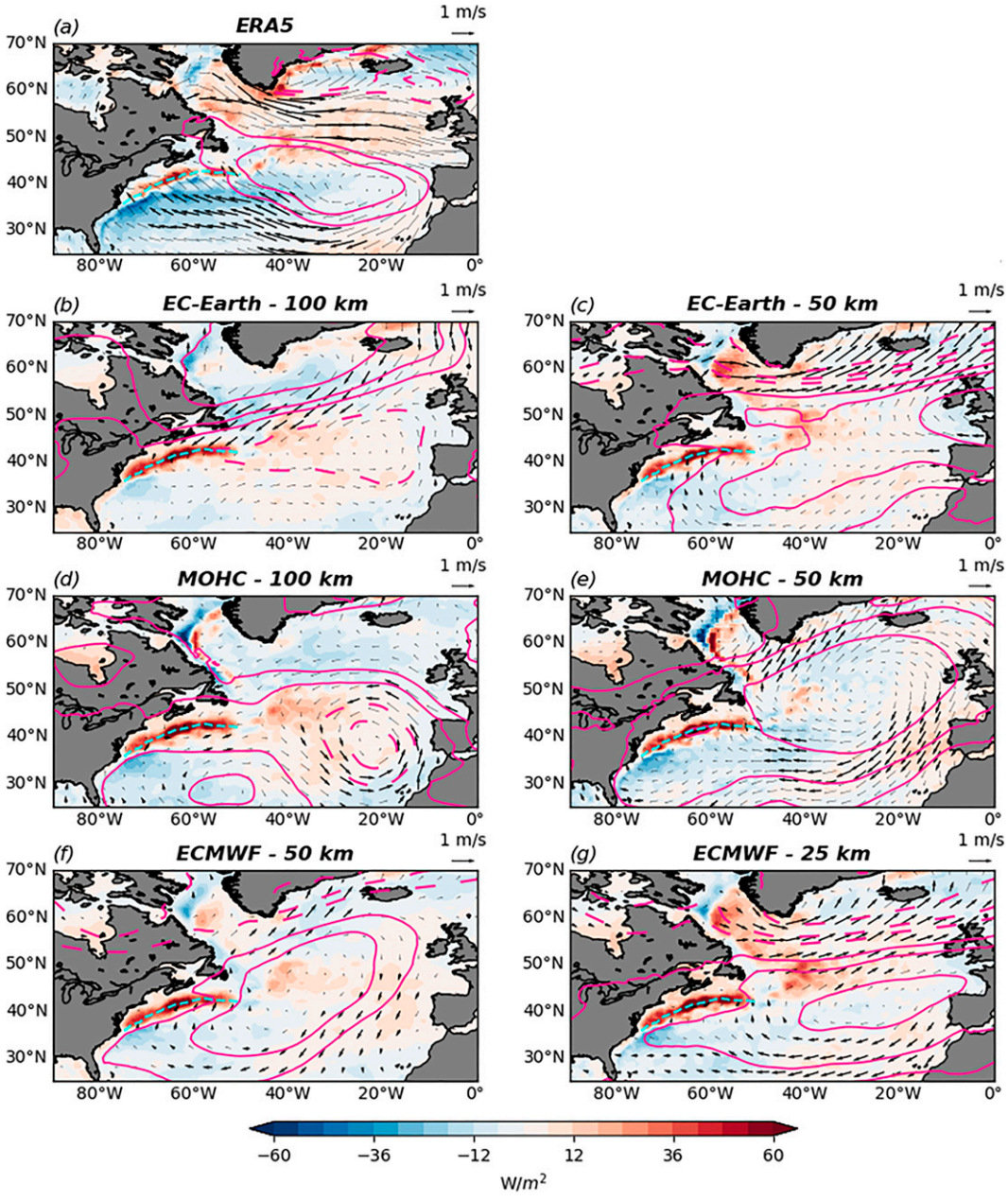

FIG. 3. Surface turbulent heat fluxes (W m^{-2}; color shading), sea level pressure (Pa; contours, solid for positive), and near-surface wind (m s^{-1}; vectors) response to the GSF shifts in winter (DJF), for (a) ERA5, (b),(c) EC-Earth, (d),(e) MOHC, and (f),(g) ECMWF. Beside each institution name, the model nominal resolution (km) is reported. Surface heat fluxes are considered to be positive upward, namely from the ocean to the atmosphere. For models the magenta contours represent sea level pressure anomalies at −120, −60, −30, 30, 60, and 120 Pa; for ERA5 the magenta contours represent sea level pressure anomalies at −180, −150, 150, and 180 Pa. Thick vectors indicate wind anomalies that were found to be significant at the 90% confidence level (details in section 2). The winter climatological position of the GSF is indicated by the cyan dashed line. The arrow in the upper-right corner of each panel is the unit vector for surface wind (m s^{-1}).

winds at 850 hPa, zonally averaged in the 0°–60°W longitudinal range and maximized in the 15°–75°N latitudinal range. Even though there are some differences between the two R100 models and between the four R50+ models, the common characteristics in each group are consistent with the results shown for the zonal wind anomalies at 850 hPa, indicating a northward shift in R50+ models and a southward shift in R100 models. Again, only the anomalies in the jet latitude distribution of the R50+ models resemble the respective observed (ERA5) anomalies, being consistently weaker than the latter. Indeed, in

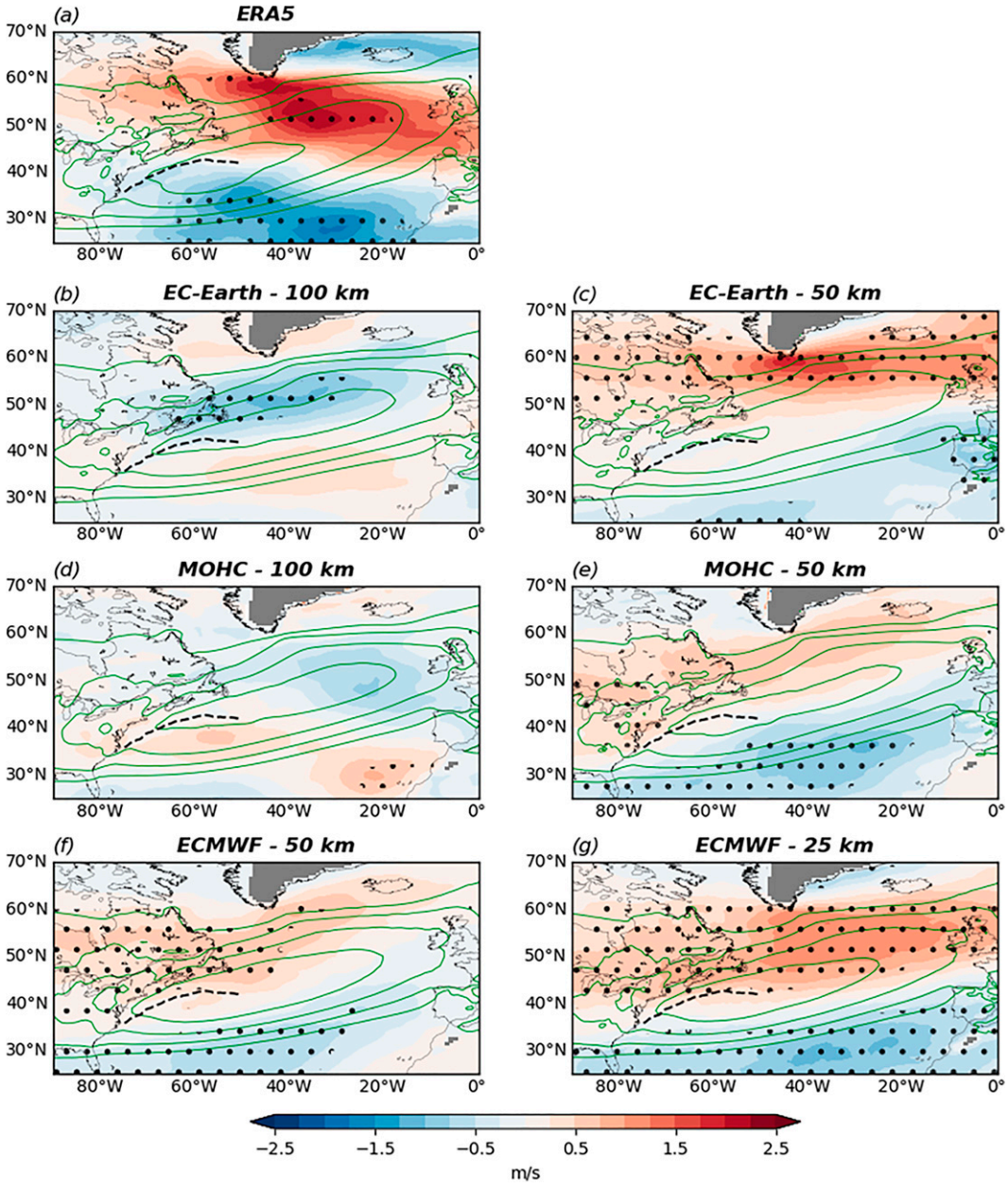

FIG. 4. 850-hPa zonal wind (m s^{-1}; color shading) response to the GSF shifts in winter (DJF): (a) ERA5, (b),(c) EC-Earth, (d),(e) MOHC, and (f),(g) ECMWF. Beside each institution name, the model nominal resolution (in km) is reported. Black dots denote anomalies that were found to be statistically significant at the 90% confidence level (details in section 2). Green contours indicate the winter climatology of zonal wind at 850 hPa every 2 m s^{-1} from 4 m s^{-1}. The winter climatological position of the GSF is indicated by the black dashed line. The gray masking corresponds to areas where the orography intersects the climatological 850-hPa isobaric surface.

ERA5 the GSF displacements are associated with anomalies of opposite sign in the jet latitude distribution north and south of the GSF position (approximately at 42°N) indicating shifts in the eddy-driven jet that are homodirectional to the GSF shifts. It should be noted that none of the six models can reproduce the trimodal character of the observed jet latitude distribution in wintertime, originally shown by Woollings et al. (2010) and seen here for ERA5. Particularly, the southern jet regime is too weakly represented by the models, a problem that is arguably linked to the absence of coupled feedbacks in atmosphere-only simulations. Models unable to represent the observed circulation regimes (Madonna et al. 2017) are also expected to feature a "distorted" response to the GSF variability as it has been noted that the atmosphere tends to respond to oceanic and other moderate forcings by changes in the frequency of occurrence of its dominant circulation regimes (Palmer 1993).

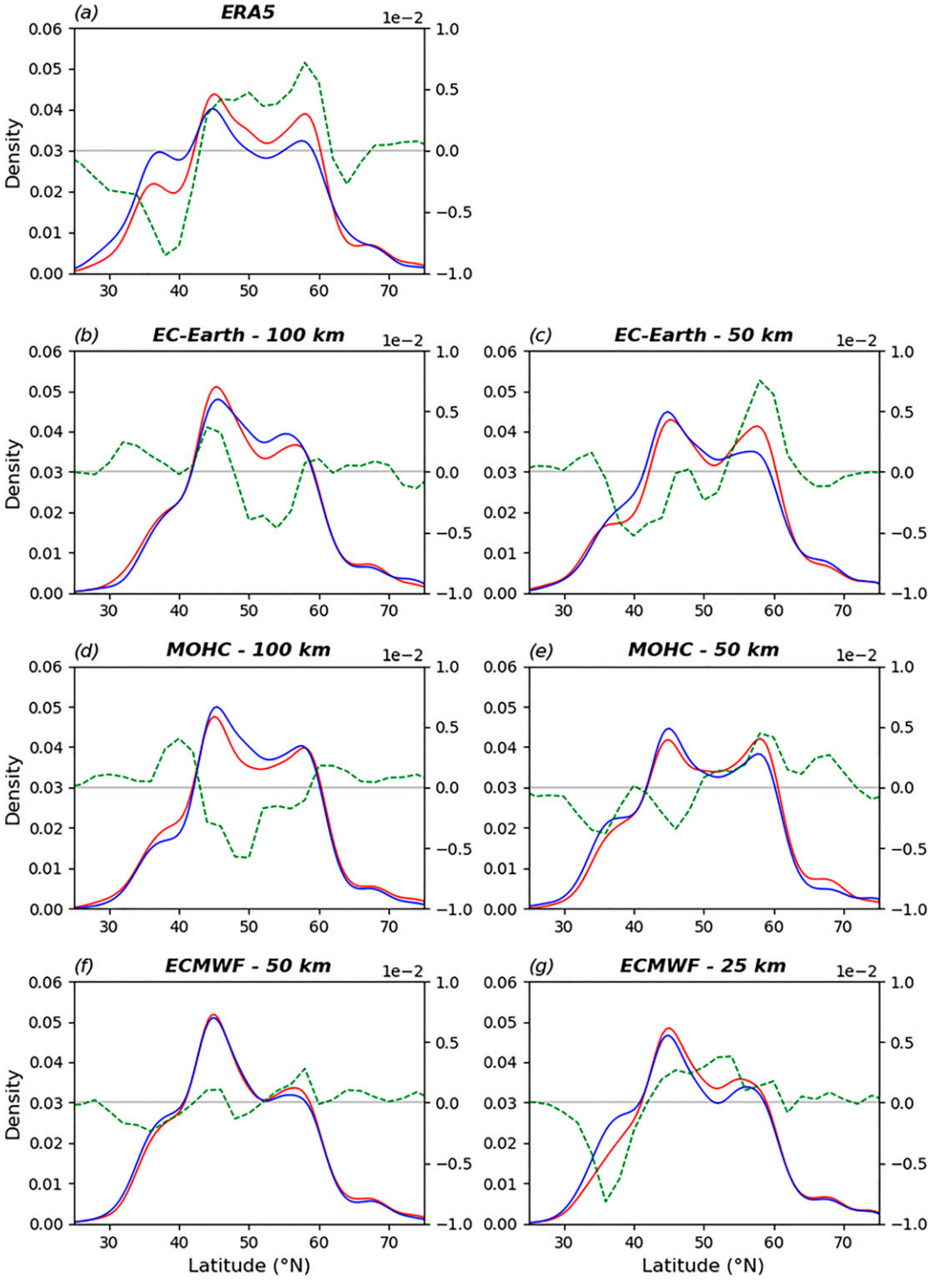

FIG. 5. Jet latitude distributions during winter (DJF): (a) ERA5, (b),(c) EC-Earth, (d),(e) MOHC, and (f),(g) ECMWF. As specified in section 2 and following the method in Woollings et al. (2010), the jet latitude has been defined through the zonal winds at 850 hPa, zonally averaged in the 0°–60°W longitudinal range and maximized in the 15°–75°N latitudinal range. Beside each institution name, the model nominal resolution (km) is reported. Red (blue) lines represent the distribution during the "North" ("South") phase of the GSF position in the respective model. Green lines represent the difference between the two distributions ("North" minus "South") and correspond to the right *y* axis.

The jet latitude variability has been previously interpreted as a response to variations in the storm track activity, which influences the jet stream through an upstream baroclinic and a downstream barotropic effect (Novak et al. 2015; O'Reilly et al. 2017). The former is based on the nonlinear oscillator relationship between low-level baroclinicity and MEHF (Ambaum and Novak 2014); the latter is the downstream representation of the upstream low-level baroclinicity changes, which induce variations in eddy anisotropy and wave breaking, with direct impact on jet latitude (Orlanski 2003). To assess whether the previously discussed homodirectional jet stream response to the GSF shifts is the result of changes in low-level baroclinicity and then in storm track activity, in Figs. 6 and 7 we show the meridional temperature gradient (here used as a proxy for baroclinicity) and MEHF anomalies at 925 and 850 hPa, respectively. As expected, the strong positive SHF anomaly (corresponding to the "North" minus "South" composites difference) along the GSF induces local changes in low-level baroclinicity both in R100 and R50+ models. Specifically, baroclinicity is found to increase at the northern flank of the GSF and to decrease at the southern flank. In the immediate vicinity of the GSF, these changes are understood as forced by the displacement of the SST front itself and are consistent with the meridional gradient of the above-mentioned SHF anomaly. Beyond these local changes, in R50+ models low-level baroclinicity undergoes significant changes also in a meridionally broader zone to the north of the GSF. As discussed later, these changes may be explained considering the meridional gradient in zonal temperature advection (dipole of opposite temperature tendencies) associated with the meridional shift in the low-level jet, i.e., stronger westerlies to north and weaker westerlies to the south, in an area where westerlies in winter are associated with cold temperature advection from the North American continent over the relatively much warmer ocean, tend to increase atmospheric baroclinicity in between. Similar large-scale anomalies in atmospheric baroclinicity have been detected also by Nakamura and Yamane (2009), who argued that SST anomalies associated with the GS variability, despite being limited to the GS area, may be responsible for such broader-scale anomalies in atmospheric baroclinicity.

Given the changes in low-level baroclinicity in the broader area to the north of the GSF (around and to the east of Newfoundland, between 45° and 55°N), R50+ models are found to respond with increased MEHF there as expected for baroclinic adjustment (Stone 1978). This can be seen clearly in Fig. 7, while it is not the case for the R100 models. This discrepancy relates to how R100 models respond (differently, as shown in the next section) to the anomalous diabatic heating along the GSF.

In turn, the increased MEHF found for R50+ models in the broader area to the north of the GSF is considered to be part of the causal chain leading to the shift of the eddy-driven jet as it indicates westward acceleration in the lower troposphere following the E-vector formulation of eddy–mean flow interaction (Hoskins et al. 1983). In fact, the storm track (diagnosed via the variance of the meridional eddy velocity aloft, $v'v'$ at 250 hPa; see Fig. S1 in the online supplemental material) is found to move with the jet as it exhibits a meridional dipole pattern of anomalies similar to the one seen for the zonal wind in R50+ models. However, the horizontal E-vector ($v'^2 - u'^2$; $-u'v'$) divergence at 250 hPa (not shown) did not reveal a significant forcing on the zonal mean flow.

The detected changes in low-level baroclinicity, MEHF, and storm activity for R50+ models are found to be similar and more pronounced in the observations (ERA5; in Figs. 6 and 7), as was the case for the zonal wind anomalies (Fig. 4). In this context it must be specified that, while in the atmosphere-only simulations the atmospheric anomalies are only a response to the oceanic forcing, the respective anomalies detected in the observations also represent the atmospheric forcing that causes the GSF shifts in the first place (at negative lags but also at lag 0; i.e., concurrent with and preceding the changes in the GSF position). The study by Frankignoul et al. (2001) is quite insightful in this regard, showing that the GS axis moves to the north (south) following positive (negative) NAO-like forcing. A follow up study is in progress analyzing the respective coupled multimodel ensemble simulations.

Finally it is specified that the low-level baroclinicity anomalies have been computed taking into account also the changes in the static stability component, yet they show patterns quite comparable to what is described above for both AGCMs and observations (not shown). This means that the low-level baroclinicity anomalies are mostly due to changes in the meridional temperature gradient rather than changes in static stability.

4. Heat budget

In the previous section it has been shown that R100 and R50+ simulations respond differently to the meridional displacements of the GSF, in terms of circulation and transient eddy activity. The resolution-dependent response of the atmospheric circulation to similar SHF anomalies close to the GSF raises the question of what might be different between R100 and R50+ models in terms of the primary, local response to the anomalous diabatic heating associated with the GSF shifts. Moreover, it was found that in R100 models cold meridional advection tends to balance the anomalous diabatic heating, while this was not found to be the case for R50+ models. Therefore, our study was naturally led to the analysis of the local thermodynamic balance.

Relevantly to this point, Smirnov et al. (2015), analyzing the response of low- and high-resolution atmosphere-only models to prescribed idealized SST forcing along an oceanic front, have found that the local heat budget depends on the horizontal resolution. Thus, to address the questions posed above, a similar analysis was conducted for each of the examined models. Specifically, the terms of the time-mean thermodynamic equation have been computed as in Smirnov et al. (2015):

$$\overline{\dot{Q}} - \underbrace{\overline{u}\frac{\partial \overline{T}}{\partial x}}_{\text{I}} - \underbrace{\frac{\partial \overline{u'T'}}{\partial x}}_{\text{II}} - \underbrace{\overline{v}\frac{\partial \overline{T}}{\partial y}}_{\text{III}} - \underbrace{\frac{\partial \overline{v'T'}}{\partial y}}_{\text{IV}} - \underbrace{\left(\overline{\omega}\frac{\partial \overline{T}}{\partial p} - \frac{k}{p}\overline{\omega}\overline{T}\right)}_{\text{V}} - \underbrace{\left(\overline{\omega'\frac{\partial T'}{\partial p}} - \frac{k}{p}\overline{\omega'T'}\right)}_{\text{VI}} = 0. \quad (1)$$

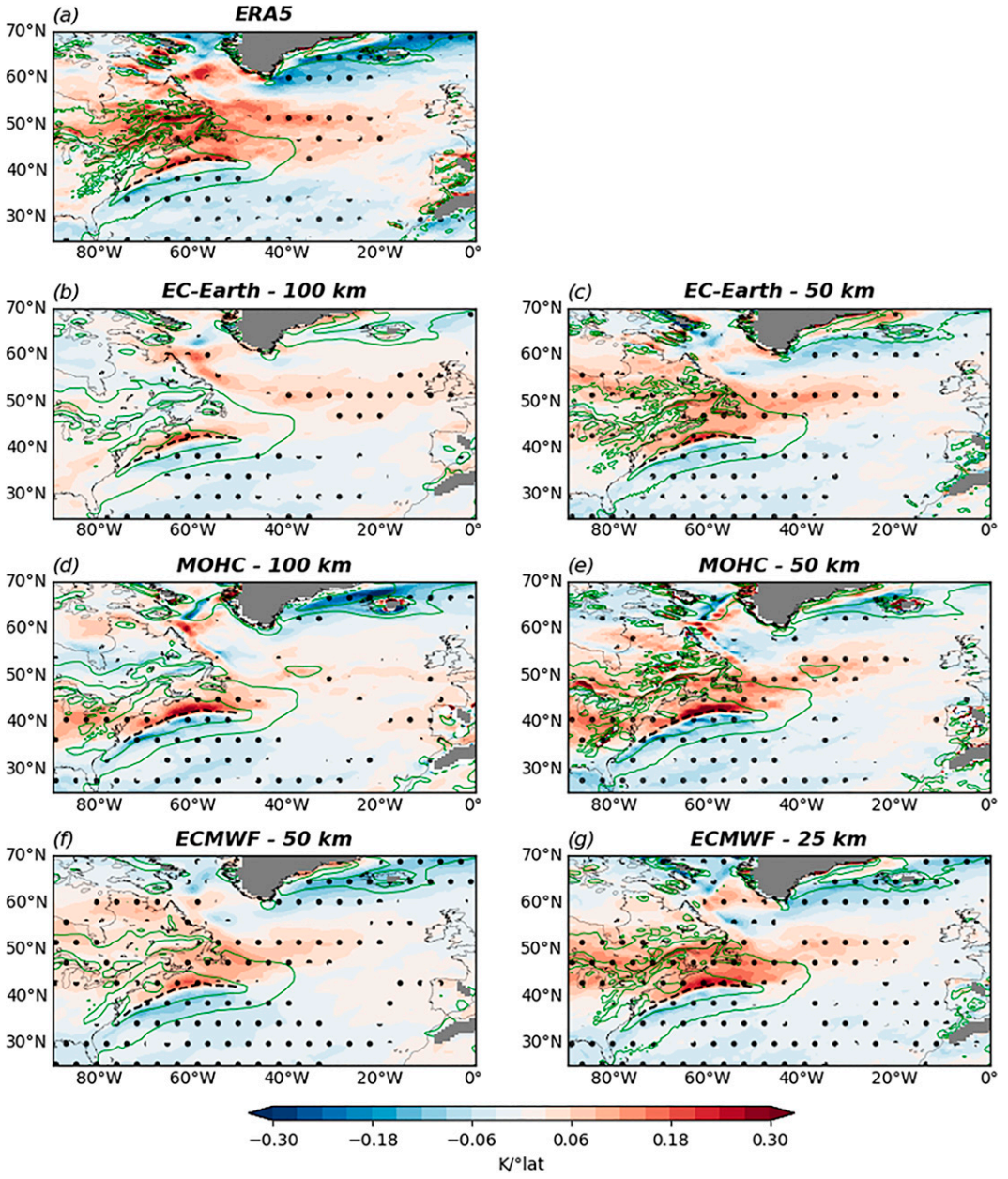

FIG. 6. 925-hPa meridional air temperature gradient (K per degree latitude; color shading) response to the GSF shifts in winter (DJF): (a) ERA5, (b),(c) EC-Earth, (d),(e) MOHC, and (f),(g) ECMWF. The temperature gradient is reversed, i.e., equatorward. Beside each institution name, the model nominal resolution (km) is reported. Black dots denote anomalies that were found to be statistically significant at the 90% confidence level (details in section 2). Green contours indicate the winter climatology every 0.8 K per degree latitude from 0.8 K per degree latitude. The winter climatological position of the GSF is indicated by the black dashed line. The gray masking corresponds to areas where the orography intersects the climatological 925-hPa isobaric surface.

Here u and v represent the zonal and meridional wind component respectively; ω is the pressure tendency, proportional to the vertical wind; p and T represent the pressure and the temperature, while $\dot{Q}$ is the diabatic heating rate. It is specified that $\dot{Q}$ is not provided as model output and that it has been calculated as a residual from the other heat budget terms. The overbars indicate climatological monthly means during winter, while the primes indicate departures thereof; $k = R/C_p$, with R equal to 287 J kg^{-1} K^{-1} and C_p equal to 1004 J kg^{-1} K^{-1}. Terms I, III, and V represent the zonal, meridional, and vertical mean thermal advection, respectively. Terms II, IV, and VI represent the respective zonal, meridional, and vertical eddy

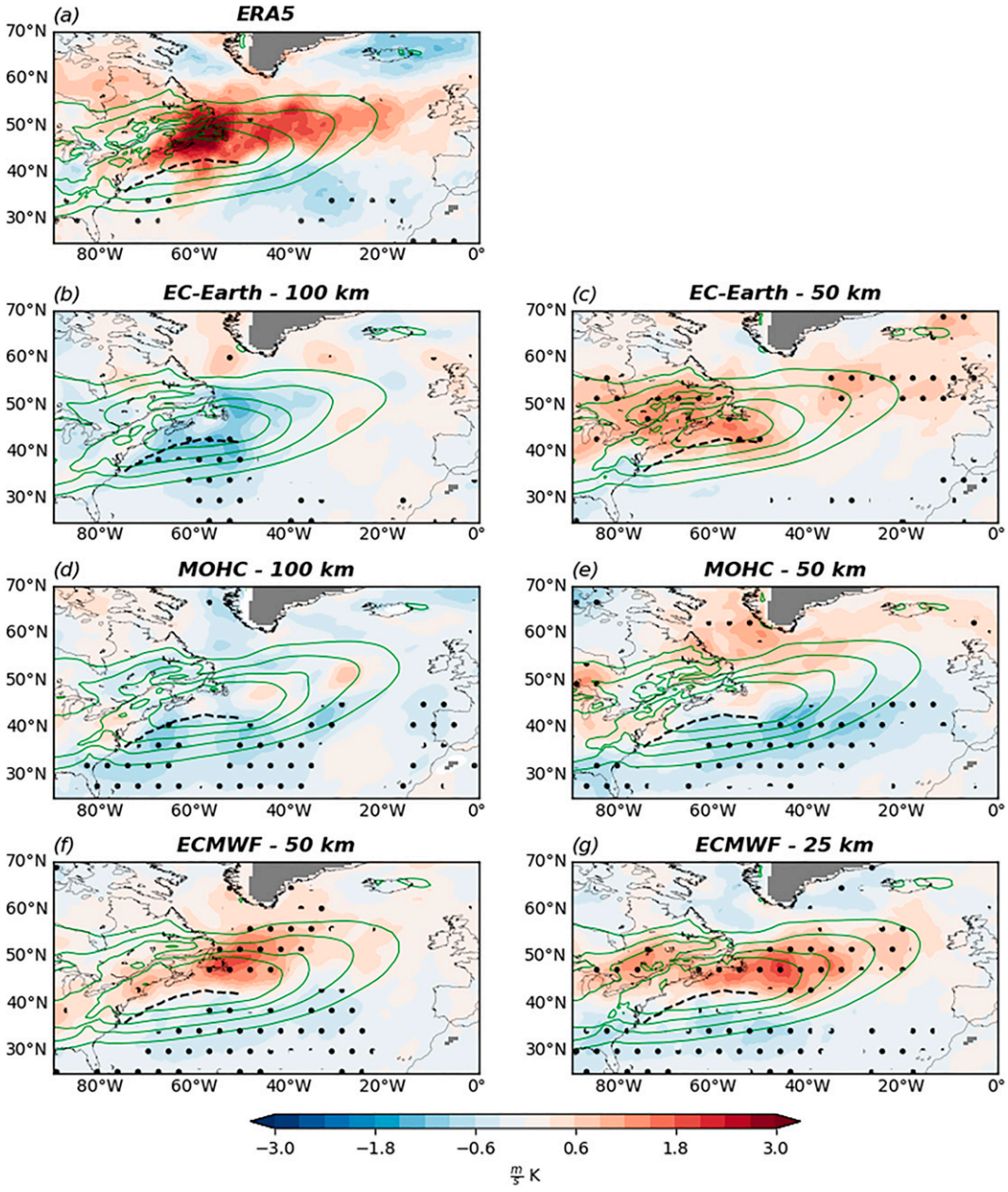

FIG. 7. Eddy heat flux anomalies ($v'T'$; m s^{-1} K; color shading) at 850 hPa induced by the GSF shifts in winter (DJF): (a) ERA5, (b),(c) EC-Earth, (d),(e) MOHC, and (f),(g) ECMWF. Beside each institution name, the model nominal resolution (in km) is reported. Black dots denote anomalies that were found to be statistically significant at the 90% confidence level (details in section 2). Green contours indicate the winter climatology of eddy heat flux at 850 hPa every 3 m s^{-1} K from 6 m s^{-1} K. The winter climatological position of the GSF is indicated by the black dashed line. The gray masking corresponds to areas where the orography intersects the climatological 850-hPa isobaric surface.

heat flux convergences. Terms V and VI also include the mean and eddy component of the adiabatic heating rate, respectively. All terms have been calculated for each winter calendar month and both positions of the GSF (i.e., "North" and "South"). Then, monthly differences between the "North" and "South" positions have been derived and averaged to form the respective winter means. Figure 8 shows the heat budget as indicated above, zonally averaged along the SST front and meridionally in the range between −1° and +1° north of the GSF position (using the previously described SST front-following coordinates). This latitude range has been chosen so as to match the meridional span of the intense SST anomalies

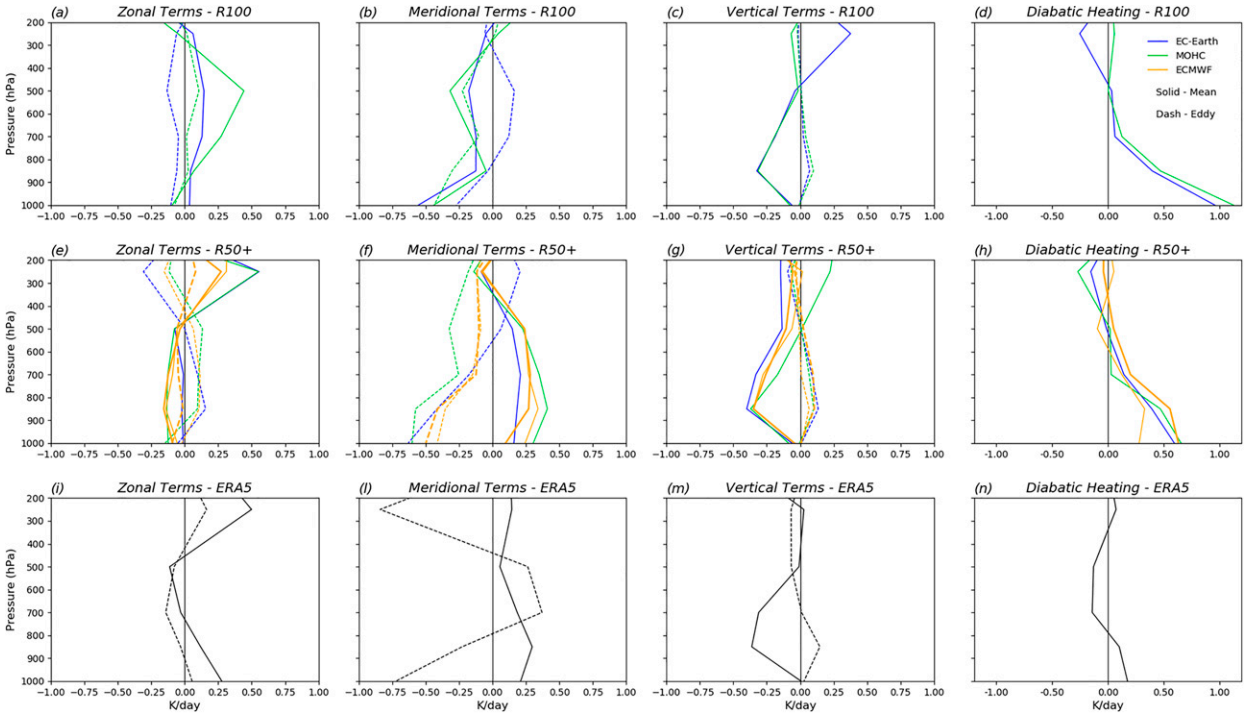

FIG. 8. Vertical profiles of composited differences for zonal (terms I and II), meridional (terms III and IV), and vertical (terms V and VI) terms in the thermodynamic budget [Eq. (1)] (K day^{-1}), for (a)–(d) R100 models, (e)–(h) R50+ models, and (i)–(n) ERA5. The last column shows the vertical profile of the diabatic heating term (K day^{-1}), calculated as residual. Each term has been calculated as a difference between the "North" and "South" phase of the GSF, averaged zonally along the front in the 50°–68°W longitudinal range and meridionally in the range −1° and +1° north of the SST front position (using the SST front-following coordinate system described in section 2). Blue lines refer to the EC-Earth model, green lines to the MOHC model, orange lines to the ECMWF model, and black lines to ERA5. Orange bold lines in (d)–(f) refer to the ECMWF model with a nominal resolution of 25 km. Solid lines refer to terms involving heat transport by time-mean fields (terms I, III, and V), while dashed lines refer to the respective eddy components of heat transport (terms II, IV, and VI).

induced by the meridional shifts of the GSF (Fig. 1) and the induced SHF anomalies (Fig. 3) in its vicinity.

At the vicinity of the GSF both the R100 and R50+ models show strong diabatic heating anomalies in the lower troposphere, below 600–700 hPa, with maximum values near the surface (Figs. 8d,h). This is expected considering the collocated positive SHF anomalies shown in Fig. 3. It is noted, also, that R100 models exhibit significantly larger diabatic heating near the surface that is largely balanced by the cold temperature advection by the mean flow in these models (Fig. 8b). Furthermore, it should be mentioned that the diabatic heating rate has been calculated as a residual from the thermodynamic equation and thus it includes other heating terms. In general, the diabatic heating in the boundary layer of a limited geographical area (as that straddling the GSF) depends on the underlying SHF (sensible and, if condensation occurs, also latent) distributed in the vertical by the boundary layer parameterization scheme, as well as to the locally absorbed radiation and the net heat fluxes entering through the lateral boundaries of the area. Considering these aspects, the diabatic heating rates shown in Figs. 8d, 8h, and 8n and in Fig. S2 are not directly comparable with the SHF shown in Fig. 3. Finally, it should be mentioned that the diabatic heating rate calculated as a residual is affected by any errors in computing all the terms in the thermodynamic budget. In ERA5 the diabatic heating in the lower troposphere is weaker than in the models (Fig. 8n; see also Fig. S2), something that is understood considering that ERA5 data come from a coupled world/model.

Near the surface the diabatic heating anomalies described above are largely balanced by horizontal heat terms, with a dominance of the meridional components (terms III and IV) over the zonal ones (terms I and II) in all cases. However, while in ERA5 and R50+ models the anomalous diabatic heating at and near the surface is balanced exclusively by the meridional eddy heat flux divergence (term IV) with the meridional mean advection (term III) opposing this action, in R100 models the meridional mean advection cooperates with the meridional eddy heat flux divergence in balancing diabatic heating (Figs. 8b,f,l). The different role played near the surface by the meridional mean advection in R50+ and R100 models, as discussed above, is consistent with the near-surface wind anomalies presented in Fig. 3, while similar differences in mechanisms balancing the heating at the surface emerged also in Smirnov et al. (2015). Vertical terms (terms V and VI) are negligible at the surface as expected for vanishing vertical

motions at the lower boundary (Figs. 8c,g,m). Instead, considering that the vertical profile of diabatic heating exhibits a gradual reduction from the surface up to about 600 hPa (Fig. 8; see also Fig. S2), it is noted that for all models and the observations (ERA5) the anomalous diabatic heating in the lower troposphere is partly balanced by mean vertical motion. In the vicinity of the GSF, which is an area of intense cyclogenesis and low-level convergence associated with the passage of frontal systems (Parfitt and Seo 2018), the "mean vertical motion" should be understood as the aggregated effect of pulses in vertical motion. Zonal terms (terms I and II) seem to play a less important role, especially in the lower troposphere where the diabatic heating takes place (Figs. 8a,e,i).

To further examine the atmospheric response in the vicinity of the GSF, in Fig. 9 we present the atmospheric circulation anomalies (composite differences: "North" minus "South") along the vertical–meridional cross section in the 50°–68°W longitudinal range. All models show upward motion anomalies directly to the south of the GSF (warm sector) and downward motion anomalies to the north, thus indicating an anomalous cell-like circulation similar in character to the one seen for the time-mean circulation (contours). The upward motion anomalies are strongest in the vicinity of the GSF and in the lower troposphere (below 600 hPa) reaching their maximum at about 850 hPa. This is in agreement with the role the mean vertical motion (term V) was found to play for the local heat budget in all models and the observations. In contrast, R100 and R50+ models differ in the meridional component of the atmospheric circulation response in proximity to the GSF. R100 models exhibit equatorward motion, while R50+ models rather show a poleward anomaly. This finding is also in agreement with the different role that the meridional mean advection (term III) was found to play for the local heat budget in the R100 and R50+ models.

Based on the results of the local thermodynamic budget and atmospheric circulation, we have extended the heat budget to the entire North Atlantic region, in order to understand more the atmospheric response on the basin scale. Here we show the results for the multimodel ensemble means of R100 and R50+ models in Figs. 10 and 11 respectively. The results for each model confirm the general features of what is described in the following and are provided in the online supplemental material. Results for ERA5 are provided in Fig. 12. It is specified that each heat term in the thermodynamic budget extended to the entire North Atlantic region has been averaged over 700–1000 hPa considering that the diabatic heating anomalies are maximum in the lower troposphere (Kallberg et al. 2005). Figures 10, 11, and 12 show that the effect induced by meridional heat terms is not limited to areas above the GSF. Indeed, the cooling (warming) effect induced by meridional mean advection (term III) in the R100 models (R50+ models and ERA5) extends farther north and downstream of the Gulf Stream (Figs. 10d, 11d, and 12d), consistent with the surface circulation anomaly shown in Fig. 3. In R100 models, such large-scale temperature tendencies are largely balanced by zonal mean advection (term I; i.e., reduced cold advection from the continent associated with reduced westerlies; Fig. 10b). On the other hand, in R50+ models and ERA5 the warming induced by meridional mean advection north and downstream the GSF is partly balanced by zonal advection of cold air coming from the inland of North America (term I; Figs. 11b and 12b) and partly by meridional eddy heat flux divergence (term IV; Figs. 11e and 12e). The former is consistent with the zonal wind intensification north of the GSF shown in Fig. 4; the latter is consistent with the northward shifts of the storm track shown in Fig. 7. In the northern portion of the North Atlantic, the effect induced by zonal mean advection is particularly intense in both models and observations. However, in R100 models the zonal mean advection is largely counterbalanced by negative diabatic heating anomalies (Fig. 10a), whereas in R50+ models and observations it is balanced partly by positive diabatic heating anomalies (Figs. 11a and 12a) and meridional eddy heat flux convergence (Fig. 11e). Also Hotta and Nakamura (2011) have shown that the eddy heat flux convergence is an important heating source at high latitudes. For both models and observations, the diabatic heating is quite consistent with SHF shown in Fig. 3. Finally, both in models and observations, it is still possible to see the cooling effect induced by vertical motion above the GSF, even if weaker because of the averaging on different vertical levels (Figs. 10f, 11f, and 12f).

Overall, the large-scale thermodynamic budget is consistent with the local heat budget. Its added value lies in highlighting which are the mechanisms maintaining the large-scale baroclinicity anomalies shown in Fig. 6, shedding light on the large-scale atmospheric circulation as discussed in more detail in section 5.

5. Discussion

The results discussed in the previous sections show that R100 and R50+ models exhibit a substantially different atmospheric response to the GSF shifts. The primary forcing for the atmosphere is the anomalous diabatic heating arising from the GSF shifts (effectively "replacing" cold waters with significantly warmer waters). The north–south displacement of the maximum SST gradient is an additional forcing directly affecting low-level baroclinicity, yet only locally. The different large-scale responses featured by R50+ (realistic response) and R100 models (unrealistic response) are linked to how these models locally react to the primary oceanic forcing (SHF anomalies) to maintain their thermodynamic balance above the GSF. In R100 models, the local diabatic heating anomalies are partly balanced by meridional mean advection, while in R50+ models the meridional mean advection plays the opposite role, thus requiring a stronger submonthly meridional eddy heat flux divergence to maintain local thermodynamic balance. Then, in R50+ models the local intensification of baroclinic eddy activity (which resembles the observed one) extends farther north and downstream of the GSF, leading to a poleward shift in the storm track and the eddy-driven jet that is homodirectional to the GSF shifts, as in the observations (ERA5). Instead, R100 models fail to reproduce this large-scale response because, in the first place, they do not

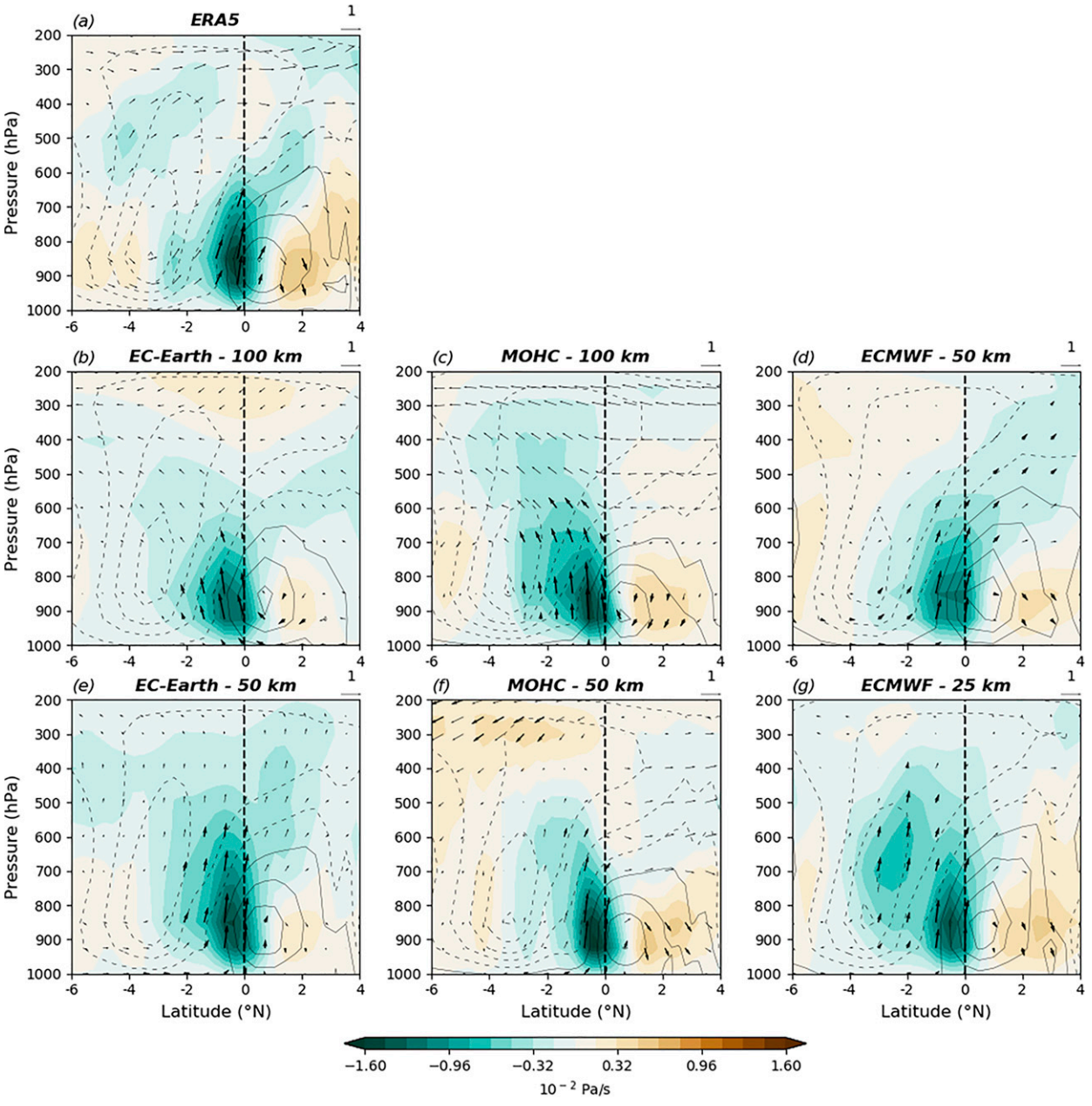

FIG. 9. Zonally averaged omega composited differences (Lagrangian pressure tendency; 10^{-2} Pa s^{-1}; color shading) and vertical–meridional winds (vectors) in response to the GSF shifts in wintertime (with the meridional wind component in m s^{-2}): (a) ERA5, (b),(e) EC-Earth, (c),(f) MOHC, and (d),(g) ECMWF. Both the terms have been zonally averaged along the SST front in the 50°–68°W longitudinal range, using the SST front-following coordinate system described in section 2. A vector scale for vertical–meridional winds is shown in the top-right corner of each panel. Beside institution name, the model nominal resolution in km is reported. Thick vectors indicate wind anomalies that were found to be significant at the 90% confidence level (details in section 2). Negative (positive) omega values correspond to upward (downward) motion. Gray contours indicate the winter climatology of vertical motion in the vicinity of the GSF; contour interval: 10^{-2} Pa s^{-1} with dashed contours for negative. The vertical dashed line represents the GSF position in relation to which the cross-front section has been constructed.

have the correct local circulation response to the diabatic heating anomalies.

Our results show that the mechanisms maintaining the local-scale and large-scale baroclinicity are different. As previous studies showed (e.g., Nakamura et al. 2004; Nakamura and Yamane 2010), differential surface heating across oceanic fronts is key in maintaining low-level baroclinicity close to the GSF against the erosive effect of baroclinic eddy fluxes. Given

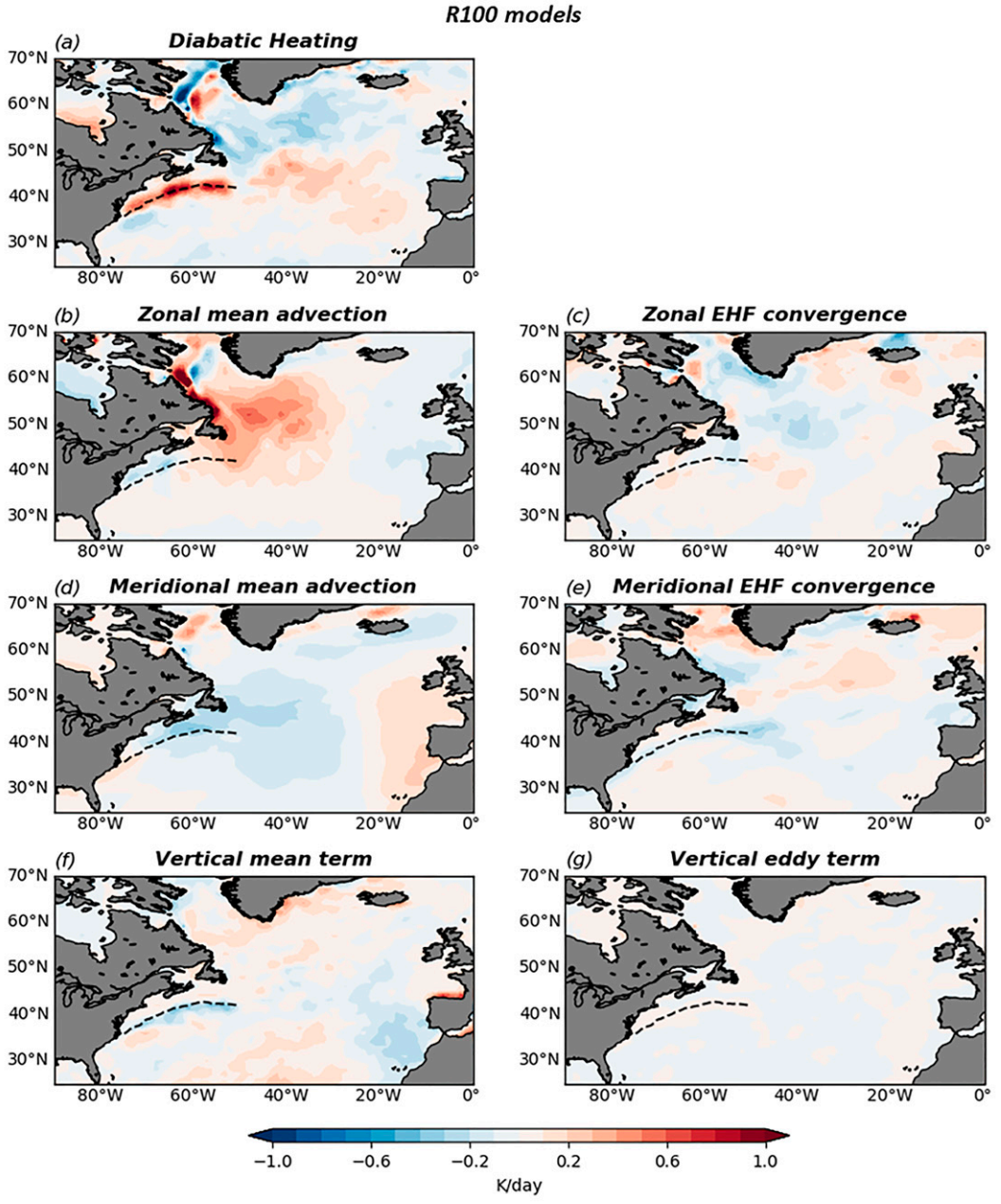

FIG. 10. Horizontal distribution of composited differences for zonal (terms I and II), meridional (terms III and IV), and vertical (terms V and VI) terms in the thermodynamic budget [Eq. (1)] (K day^{-1}), averaged over 700–1000 hPa, as ensemble mean of models with a nominal resolution of 100 km (R100 models). (a) Diabatic heating. (b) Zonal mean advection (term I). (c) Zonal eddy heat flux (EHF) convergence (term II). (d) Meridional mean advection (term III). (e) Meridional EHF convergence (term IV). (f) Vertical mean term (term V). (g) Vertical eddy term (term VI). The winter climatological position of the GSF is indicated by the black dashed line.

that the GSF shifts are quite limited in meridional distance (approximately 50–100 km as indicated by Fig. 2 for the two tercile categories), the zone of maximum atmospheric baroclinicity is expected to shift with the GSF by a similar distance. Therefore, this effect alone cannot explain the detected large-scale baroclinicity anomalies. The detected large-scale changes in low-level baroclinicity in R50+ and in ERA5 can be explained by the differential zonal temperature advection induced by the detected changes in zonal wind near the east coast of the North American continent. Given that in that area (around and east of Newfoundland) in winter there is strong cold advection by the westerly flow, stronger westerlies to the

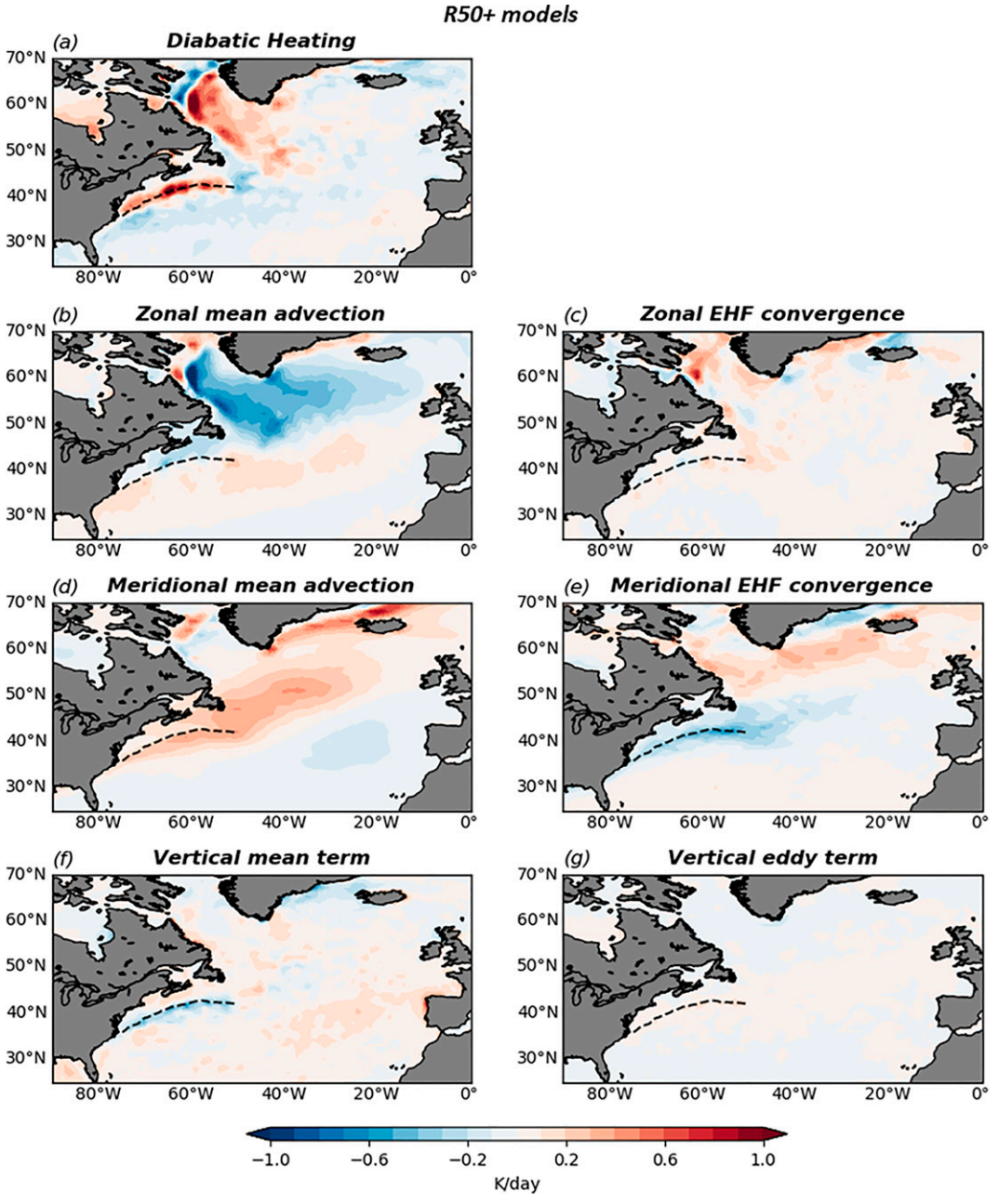

FIG. 11. Horizontal distribution of composited differences for zonal (terms I and II), meridional (terms III and IV), and vertical (terms V and VI) terms in the thermodynamic budget [Eq. (1)] (K day^{-1}), averaged over 700–1000 hPa, as the ensemble mean of models with a nominal resolution greater than 50 km (R50+ models). (a) Diabatic heating. (b) Zonal mean advection (term I). (c) Zonal eddy heat flux (EHF) convergence (term II). (d) Meridional mean advection (term III). (e) Meridional EHF convergence (term IV). (f) Vertical mean term (term V). (g) Vertical eddy term (term VI). The winter climatological position of the GSF is indicated by the black dashed line.

north and weaker westerlies to the south (as in Fig. 4) imply a differential temperature tendency (Figs. 11 and 12) that tends to increase baroclinicity in between (Fig. 6). We suggest that there is a positive feedback between the intensification of the MEHF and the large-scale zonal wind anomalies, triggered by the local atmospheric response in the vicinity of the GSF.

In this context, another point that requires discussion is what causes the detected shift in the storm track and the jet (referring to R50+ and ERA5). The respective anomalies in MEHF shown in Fig. 7 are, indeed, consistent with collocated changes in the low-level jet following eddy–mean flow interaction arguments (Hoskins et al. 1983; Novak et al. 2015). The

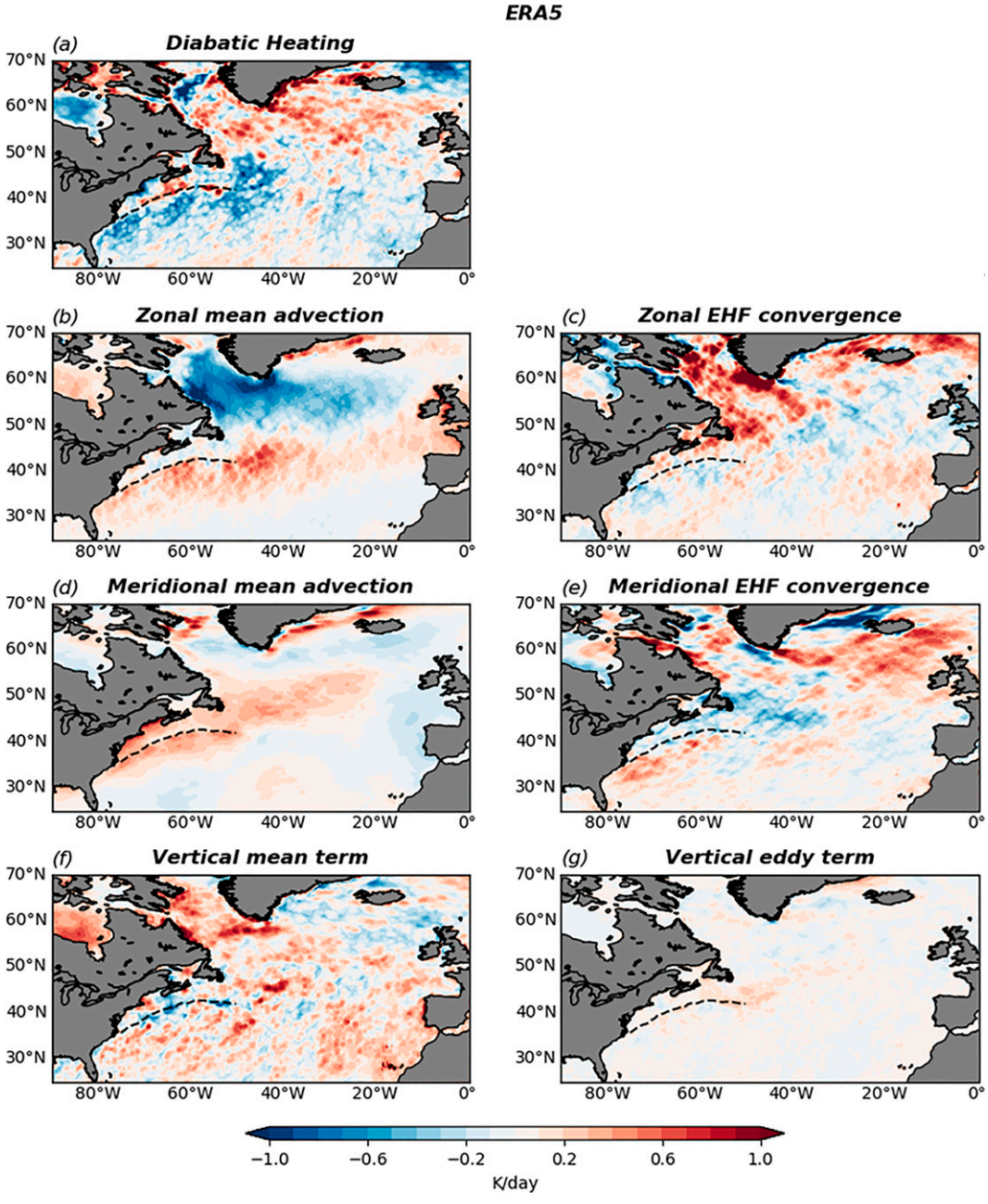

FIG. 12. Horizontal distribution of composited differences for zonal (terms I and II), meridional (terms III and IV), and vertical (terms V and VI) terms in the thermodynamic budget [Eq. (1) (K day^{-1}), averaged over 700–1000 hPa, for ERA5. (a) Diabatic heating. (b) Zonal mean advection (term I). (c) Zonal eddy heat flux (EHF) convergence (term II). (d) Meridional mean advection (term III). (e) Meridional EHF convergence (term IV). (f) Vertical mean term (term V). (g) Vertical eddy term (term VI). The winter climatological position of the GSF is indicated by the black dashed line.

former, however, cannot fully explain the pattern of the zonal wind anomalies (Fig. 4), while the divergence of the horizontal E-vector components aloft (not shown) was not found to play the expected role aiding the understanding of the changes in the jet. In contrast, the analysis of atmospheric blocking was found to be insightful as the detected anomalies are dynamically consistent with the jet and storm track changes. Figure 13 shows blocking frequency anomalies associated with the GSF shifts (composite differences "North" minus "South," as for the other diagnostics). The reduced blocking frequency over Greenland seen for R50+ and ERA5 is in agreement with a northerly displaced jet and storm track, as Greenland

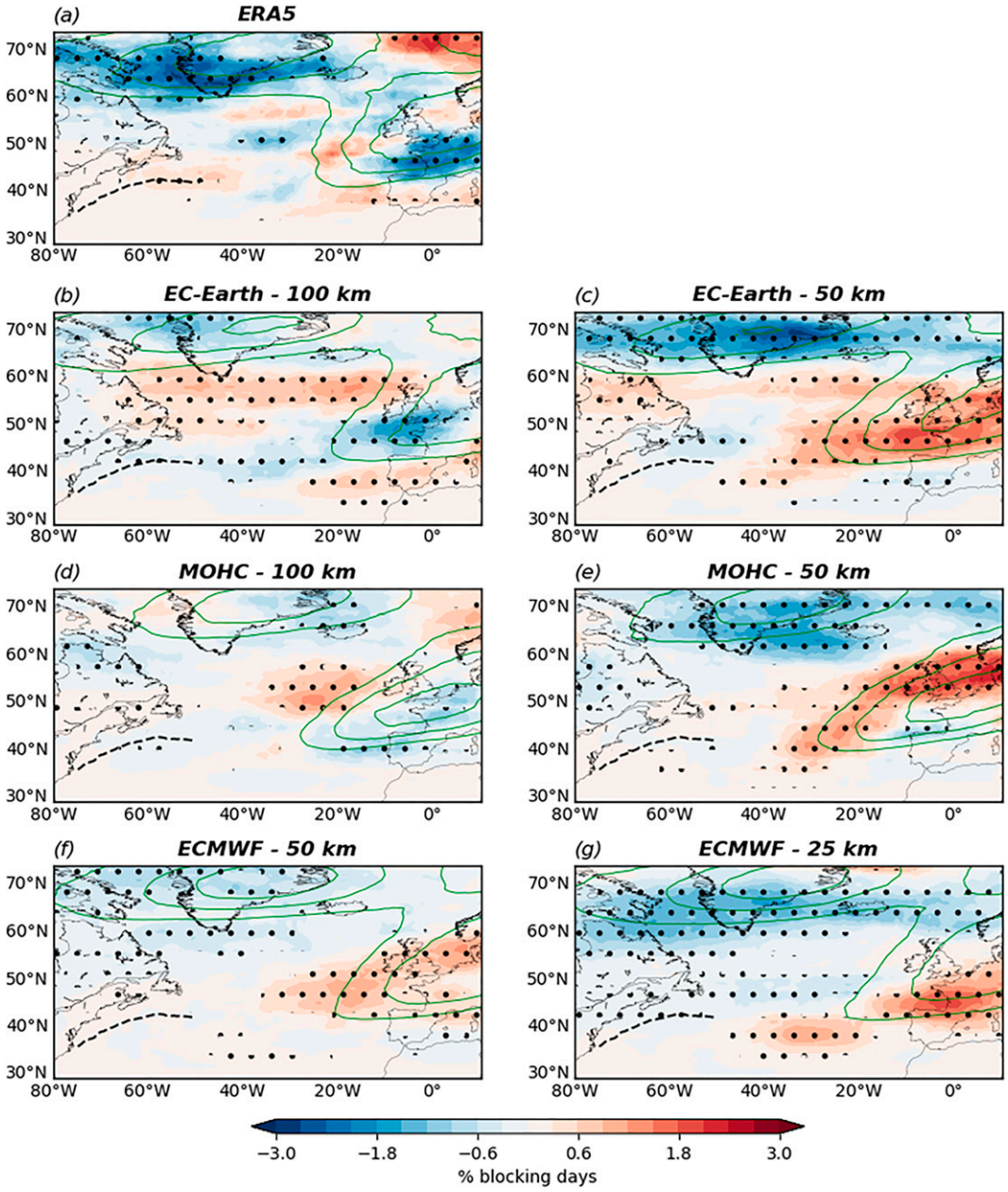

FIG. 13. Blocking frequency anomalies (% of blocked days on total days; color shaded) induced by the GSF shifts in winter (DJF): (a) ERA5, (b),(e) EC-Earth, (c),(f) MOHC, and (d),(g) ECMWF. Beside each institution name, the model nominal resolution (km) is reported. Black dots denote anomalies that were found to be statistically significant at the 90% confidence level (details in section 2). Green contours indicate the winter climatology of blocking frequency every 2% from 4.5%. The winter climatological position of the GSF is indicated by a black dashed line.

blocking tends to displace the jet to the south leading to higher occurrences in the southern-jet regime (Woollings and Hoskins 2008; Woollings et al. 2010; Madonna et al. 2017). Our findings are very much in agreement with Joyce et al. (2019), who showed that periods of northerly GS path are associated with a reduction in Greenland blocking frequency and increased excursions of the storm track to the northeast over the Labrador Sea (namely, a poleward shift). Apart from the reduction in high-latitude blocking frequency, the observations show opposite anomalies over the European continent. Such anomalies are dynamically consistent with the enhanced zonal winds over the central-western European coast (Fig. 4a) and the higher occurrence of both the central- and the northern-jet regimes (Fig. 5a) in ERA5.

Before closing this discussion it should be mentioned that although the methodology adopted in this study aimed at isolating the oceanic forcing related to the GSF meridional shifts, the atmospheric response to this variability may be

contaminated by concurrent oceanic influences from other parts of the global ocean. To assess this possibility the authors first examined the global SST composites on the "North" and "South" tercile categories defined via the GSF position and found, in fact, ENSO-like anomalies with amplitudes reaching 0.4 K in the eastern equatorial Pacific (not shown). Consistent with these SST anomalies, Fig. S9 shows negative (positive) SLP anomalies over the western (eastern) tropical Pacific in all model simulations. On the other hand, no significant SST and SLP anomalies are found over the tropical Pacific in the ERA5 dataset. To assess the possibility of a dominant ENSO influence, the zonal wind has been linearly regressed onto ENSO (Niño-3.4 index) and then the composite differences for the zonal wind at 850 hPa (Fig. 4) have been repeated after having removed the linearly regressed zonal wind from the original data. For the models it was found that the general character and the amplitude of the detected atmospheric response in the North Atlantic is largely insensitive to this test (not shown). In ERA5 the results indicate a northward shift of the eddy-driven jet, with an amplitude and statistical significance greater than the one in the original analysis. Since no ENSO-like anomalies are present in the tropical Pacific in ERA5, such differences are understood as the effect of other phenomena concurrent with ENSO. However, excluding completely all possible influences from remote parts of the global ocean is practically impossible as the historical atmosphere-only simulations are forced with global observed SST fields. There exist elaborate statistical methods for defining a GSF signal with minimal contamination by other specific processes (such as the ENSO variability), yet it is not possible to exclude every potential influence foreign to the GSF variability. As an example, Fig. S9 shows SLP anomalies associated with the GSF shifts that are statistically significant over various areas of the Northern Hemisphere. For this, one would need to repeat all simulations with observed SSTs in the area of interest and climatological SSTs elsewhere.

6. Conclusions

The objective of the present work was twofold. First, the study aimed at assessing the atmospheric response to meridional shifts in the GSF via the use of multimodel atmosphere-only simulations forced with observed SSTs. Using multiple realizations for each model was key in letting the forced signal emerge from the chaotic atmospheric variability, while comparing results between different models and the observations enhanced our confidence in the interpretation of the findings. In turn, the use of atmosphere-only simulations allowed us to study the atmospheric response to the oceanic forcing in isolation, that is, focusing on a single direction of the two-way interaction between the two realms. These choices allowed the present study to provide robust evidence on how the observed GSF variability may be impacting the North Atlantic midlatitude atmospheric circulation. Second, the present study aimed at assessing the role of atmospheric horizontal resolution for the realistic simulation of the above-discussed response. In fact, past studies (e.g., Smirnov et al. 2015) have examined the dependence on model resolution of the atmospheric response to idealized SST forcings mimicking the meridional shift of an oceanic front, yet our study does so for realistic SST anomalies and in the more robust context of a multimodel, protocol-driven, coordinated framework. Here we refer to model configurations with a nominal resolution coarser than 50 km as R100 models, and those with a nominal resolution finer than or equal to 50 km as R50+ models.

The main findings can be summarized as follows. The interannual variability in the meridional position of the GSF was found to relate to intense localized SST anomalies, positive for the "North" position and negative for the "South" position (Fig. 1). These SST anomalies later induce collocated anomalies in SHF (sensible and latent) representing an important portion (15%–20%) of the winter SHF climatology over a significant area (Fig. 3). This anomalous diabatic heating forces a local atmospheric circulation response, which is fundamentally different between R100 and R50+ models. The response in the latter was found to be similar to the respective observed anomalies, which is not the case for R100 models. Discussing first the local response of the R50+ models, it was found that in the presence of the anomalous diabatic heating along the GSF, thermodynamic balance near the surface is maintained mainly by anomalous meridional eddy heat flux divergence (Fig. 8f), while the anomalous meridional mean advection [term III in Eq. (1)] tends to exacerbate the temperature tendency induced by the heating. Anomalous vertical motion is generated (Fig. 9) and this contributes significantly to counterbalancing the anomalous heating in the lower troposphere (Fig. 8g). Effectively, the baroclinic eddy activity is modified to equilibrate the anomalous baroclinicity close to the GSF, possibly intensifying the zonal winds north of the GS. This is consistent with the detected large-scale changes in low-level baroclinicity (Fig. 6), which is indeed mostly maintained by advection of cold air from inland of North America (Figs. 11 and 12; see also Figs, S4, S6, S7, and S8). Given the latter, in response through baroclinic adjustment, the baroclinic eddy activity is further intensified. As a result, the eddy-driven jet is also modified (Fig. 4) through the action of the synoptic eddy fluxes (vertical divergence of E-vectors). Finally, the detected changes in blocking frequency (Fig. 13) are dynamically consistent with the changes in the storm track and the jet and in agreement with previous findings (Joyce et al. 2019). To conclude, R50+ models produce a local as well as a large-scale atmospheric circulation response with patterns similar to the respective observed anomalies. The latter consist of a shift in the North Atlantic eddy-driven jet and storm track that is homodirectional to the GSF shifts (Fig. 5). Low-resolution (R100) models produce a strongly different local circulation response to the anomalous diabatic heating associated with the GSF shifts. It is argued that these differences in the local circulation response are key to understanding the differences in the large-scale response detected in these models. Arguably, the most important of the above-mentioned aspects is that R100 models were found to maintain thermodynamic balance near the surface not through an intense anomaly in meridional eddy heat transport but through the action of anomalous meridional mean temperature advection (Fig. 14). This does not agree with the

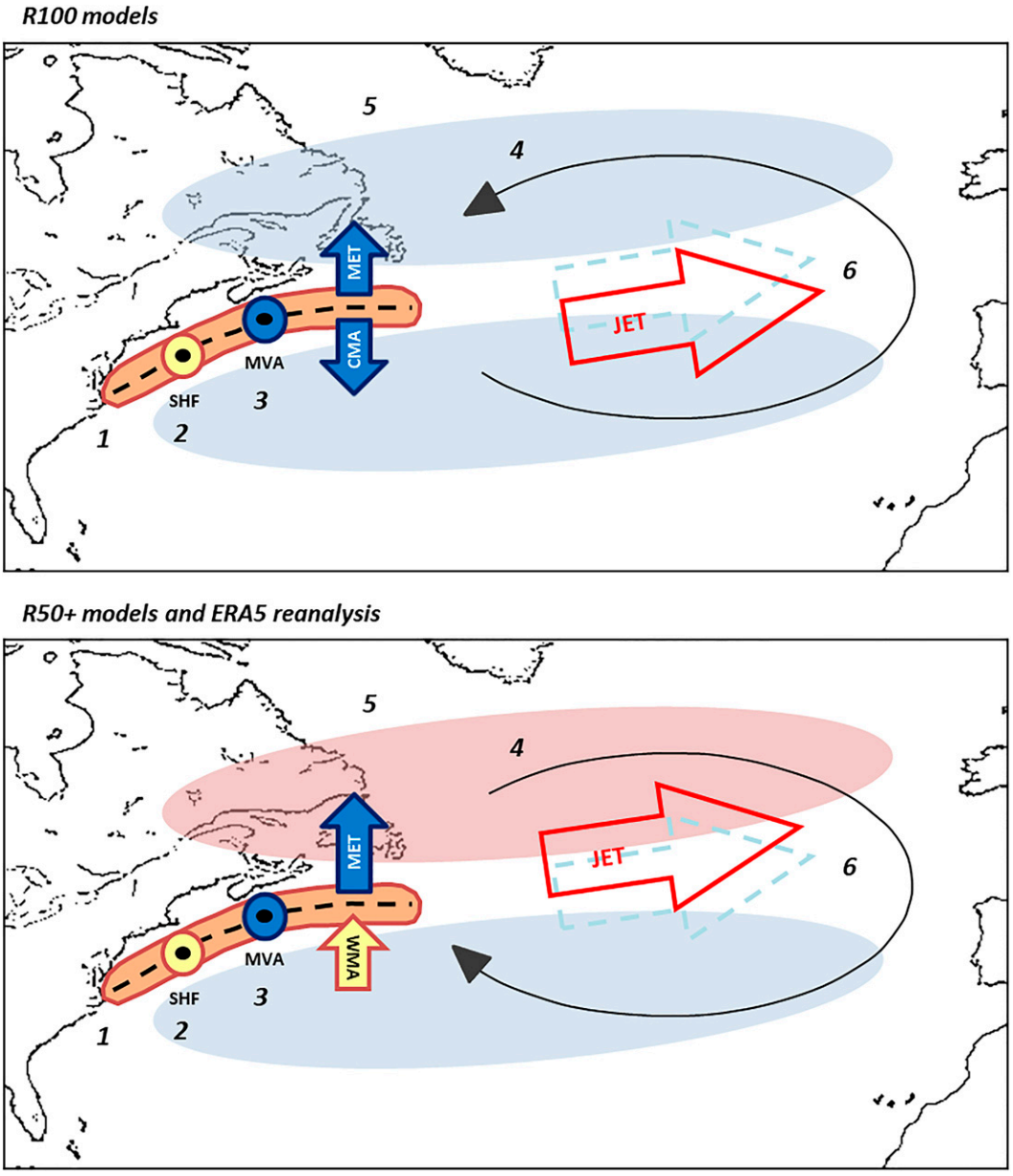

FIG. 14. Schematic of the atmospheric response to the GSF shifts in winter for (top) R100 models and (bottom) R50+ models and the ERA5 reanalysis. The winter climatological position of the GSF is represented by the black dashed line. 1) The brown zone straddling the GSF represents the area of intense SST anomalies induced by a shift of the oceanic front from its "South" to its "North" position. 2) The strong alongfront SST anomalies induce intense anomalies in surface heat fluxes (SHF), represented by yellow circles with a black point in the center, meaning that the ocean is warming the atmosphere. 3) In R100 models the diabatic heating anomaly in the vicinity of the GSF is largely balanced by mean vertical advection (MVA), meridional eddy heat transport (MET; with "eddy" meaning monthly departures from climatology), and cold meridional advection (CMA). In R50+ models MVA has a similar role, but the warm meridional advection (WMA) induces a positive temperature tendency. Thus, to maintain balance, MET is significantly stronger than in R100 models. The direction of the arrows in respect to the GSF is supposed to indicate heat transport convergence (warming for WMA; yellow) and divergence (cooling for MET and CMA; blue). 4) Downstream of the GSF, the R100 (R50+) models exhibit surface cyclonic (anticyclonic) circulation anomalies consistent with the CMA and WMA, respectively. 5) In R100 models the GSF shifts are associated with a reduction in synoptic eddy heat fluxes ($v'T'$) in most of the North Atlantic, whereas R50+ models exhibit positive (negative) anomalies north (south) of the GSF, represented by the red (blue) shadows. 6) The eddy-driven jet shifts poleward (equatorward) in R50+ (R100) models.

circulation changes found in the observations and in high-resolution (R50+) models. It is plausible that the improvement of the response in high-resolution models is conveyed by a better representation of mesoscale ocean-to-atmosphere forcing that is not resolved in their low-resolution counterparts and/or a more realistic representation of small-scale key atmospheric features, such as fronts and conveyor belts. After all, it should be remembered that the atmosphere does not interact with a smooth and quasi-linear time mean SST front but with a much more convoluted, time-evolving SST front with gradients that are even more pronounced locally. In the comparison between AGCMs and observations, it should be pointed out that in ERA5 the atmospheric anomalies associated with concurrent GSF shifts are, at least in part, the representation of the atmospheric forcing that caused the GSF shifts. This is in line with previous studies (Taylor and Stephens 1998; Frankignoul et al. 2001; Sanchez-Franks et al. 2016) showing that the GSF latitude is positively correlated with the NAO at zero and at negative lags (NAO leading). Therefore, in contrast to the AGCMs, the concurrent atmospheric anomalies in ERA5 cannot be interpreted purely as an atmospheric response to the GSF shifts. Considering this important disparity between AGCMs and ERA5, the larger amplitude of the atmospheric anomalies detected in ERA5 compared to the anomalies in the R50+ models (e.g., see Fig. 4) is indicative of a positive feedback between ocean and atmosphere: as soon as the GSF shift is established the associated SST anomalies tend to force an NAO-like response (as the R50+ models indicate) that strengthens and/or prolongs the original atmospheric forcing (present only in ERA5). Notably, the existence of a positive feedback of this kind, i.e., between the NAO-induced tripole SST anomalies (recalling the SST anomalies associated with GSF shifts) and the NAO, has been proposed also by other authors (Czaja and Frankignoul 2002; Joyce et al. 2019). However, such a positive feedback is not confirmed by Wills et al. (2016), who found that the atmospheric variability pattern forcing SST changes in the Gulf Stream Extension area and the atmospheric anomalies subsequently forced by the same SST changes are spatially anticorrelated and temporally distant. Such discrepancies show that the character of the atmospheric response to SST anomalies near the GSF should be further investigated in the observations. This is especially true for monthly and shorter time scales, when the atmospheric variability is expected to be dominated by internal atmospheric processes, which could hamper the emergence of the atmospheric response to SST variability.

Acknowledgments. PJA and AB acknowledge funding from the PRIMAVERA project, funded by the European Union's Horizon 2020 programme under Grant Agreement 641727. During this study PA and AB received also funding by MUR–Ministero dell'Università e Ricerca (D.D. n.1316, 08/06/2021), and JPI Oceans and JPI Climate Joint Call 2019 "Next Generation Climate Science in Europe for Oceans" ROADMAP Project.

Data availability statement. All data from PRIMAVERA HighResMIP simulations used in this study are freely accessible from the Earth System Grid Federation (ESGF). The HadISST2 high-resolution SST data used (1950–2014) are also available from the ESGF (https://doi.org/10.22033/ESGF/input4MIPs.1221). ERA5 reanalysis data are available from the European Centre for Medium-Range Weather Forecasting (ECMWF).

REFERENCES

Ambaum, M. H. P., and L. Novak, 2014: A nonlinear oscillator describing storm track variability. *Quart. J. Roy. Meteor. Soc.*, **140**, 2680–2684, https://doi.org/10.1002/qj.2352.

Athanasiadis, P. J., and Coauthors, 2014: The representation of atmospheric blocking and the associated low-frequency variability in two seasonal prediction systems. *J. Climate*, **27**, 9082–9100, https://doi.org/10.1175/JCLI-D-14-00291.1.

——, S. Yeager, Y.-O. Kwon, A. Bellucci, D. W. Smith, and S. Tibaldi, 2020: Decadal predictability of North Atlantic blocking and the NAO. *npj Climate Atmos. Sci.*, **3**, 20, https://doi.org/10.1038/s41612-020-0120-6.

Bellucci, A., and Coauthors, 2021: Air–sea interaction over the Gulf Stream in an ensemble of HighResMIP present climate simulations. *Climate Dyn.*, **56**, 2093–2111, https://doi.org/10.1007/s00382-020-05573-z.

Brayshaw, D., B. Hoskins, and M. Blackburn, 2011: The basic ingredients of the North Atlantic storm track. Part II: Sea surface temperatures. *J. Atmos. Sci.*, **68**, 1784–1805, https://doi.org/10.1175/2011JAS3674.1.

Cayan, D. R., 1992: Latent and sensible heat flux anomalies over the northern oceans: The connection to monthly atmospheric circulation. *J. Climate*, **5**, 354–369, https://doi.org/10.1175/1520-0442(1992)005<0354:LASHFA>2.0.CO;2.

Ciasto, L. M., and D. W. J. Thompson, 2004: North Atlantic atmosphere–ocean interaction on intraseasonal time scales. *J. Climate*, **17**, 1617–1621, https://doi.org/10.1175/1520-0442(2004)017<1617:NAAIOI>2.0.CO;2.

Czaja, A., and C. Frankignoul, 2002: Observed impact of Atlantic SST anomalies on the North Atlantic Oscillation. *J. Climate*, **15**, 606–623, https://doi.org/10.1175/1520-0442(2002)015<0606:OIOASA>2.0.CO;2.

——, ——, S. Minobe, and B. Vannière, 2019: Simulating the midlatitude atmospheric circulation: What might we gain from high-resolution modeling of air–sea interactions? *Curr. Climate Change Rep.*, **5**, 390–406, https://doi.org/10.1007/s40641-019-00148-5.

Davini, P., C. Cagnazzo, S. Gualdi, and A. Navarra, 2012: Bidimensional diagnostics, variability, and trends of Northern Hemisphere blocking. *J. Climate*, **25**, 6496–6509, https://doi.org/10.1175/JCLI-D-12-00032.1.

Deser, C., M. A. Alexander, S. P. Xie, and A. S. Phillips, 2010: Sea surface temperature variability: Patterns and mechanisms. *Annu. Rev. Mar. Sci.*, **2**, 115–143, https://doi.org/10.1146/annurev-marine-120408-151453.

Dong, S., and K. A. Kelly, 2004: Heat budget in the Gulf Stream region: The importance of heat storage and advection. *J. Phys. Oceanogr.*, **34**, 1214–1231, https://doi.org/10.1175/1520-0485(2004)034<1214:HBITGS>2.0.CO;2.

Duchon, C. E., 1979: Lanczos filtering in one and two dimensions. *J. Appl. Meteor. Climatol.*, **18**, 1016–1022, https://doi.org/10.1175/1520-0450(1979)018<1016:LFIOAT>2.0.CO;2.

Feliks, Y., M. Ghil, and E. Simonnet, 2004: Low-frequency variability in the midlatitude atmosphere induced by an oceanic

thermal front. *J. Atmos. Sci.*, **61**, 961–981, https://doi.org/10.1175/1520-0469(2004)061<0961:LVITMA>2.0.CO;2.

——, ——, and A. W. Robertson, 2011: The atmospheric circulation over the North Atlantic as induced by the SST field. *J. Climate*, **24**, 522–542, https://doi.org/10.1175/2010JCLI3859.1.

Frankignoul, C., and K. Hasselmann, 1977: Stochastic climate models, Part II: Application to sea-surface temperature anomalies and thermocline variability. *Tellus*, **29**, 289–305, https://doi.org/10.3402/tellusa.v29i4.11362.

——, G. de Coëtlogon, T. M. Joyce, and S. Dong, 2001: Gulf Stream variability and ocean–atmosphere interactions. *J. Phys. Oceanogr.*, **31**, 3516–3529, https://doi.org/10.1175/1520-0485(2002)031<3516:GSVAOA>2.0.CO;2.

Haarsma, R. J., and Coauthors, 2016: High Resolution Model Intercomparison Project (HighResMIP v1.0) for CMIP6. *Geosci. Model Dev.*, **9**, 4185–4208, https://doi.org/10.5194/gmd-9-4185-2016.

——, and Coauthors, 2020: HighResMIP versions of EC-EARTH: EC-EARTH3P and EC719 EARTH3P-HR. Description, model performance, data handling and validation. *Geosci. Model Dev.*, **13**, 3507–3527, https://doi.org/10.5194/gmd-13-3507-2020.

Hersbach, H., and Coauthors, 2020: The ERA5 global reanalysis. *Quart. J. Roy. Meteor. Soc.*, **146**, 1999–2049, https://doi.org/10.1002/qj.3803.

Hoskins, B. J., and D. J. Karoly, 1981: The steady linear response of a spherical atmosphere to thermal and orographic forcing. *J. Atmos. Sci.*, **38**, 1179–1196, https://doi.org/10.1175/1520-0469(1981)038<1179:TSLROA>2.0.CO;2.

——, and P. J. Valdes, 1990: On the existence of storm-tracks. *J. Atmos. Sci.*, **47**, 1854–1864, https://doi.org/10.1175/1520-0469(1990)047<1854:OTEOST>2.0.CO;2.

——, I. N. James, and G. H. White, 1983: The shape, propagation and mean-flow interaction of large-scale weather systems. *J. Atmos. Sci.*, **40**, 1595–1612, https://doi.org/10.1175/1520-0469(1983)040<1595:TSPAMF>2.0.CO;2.

Hotta, D., and H. Nakamura, 2011: On the significance of the sensible heat supply from the ocean in the maintenance of the mean baroclinicity along storm tracks. *J. Climate*, **24**, 3377–3401, https://doi.org/10.1175/2010JCLI3910.1.

Joyce, T. M., C. Deser, and M. A. Spall, 2000: The relation between decadal variability of subtropical mode water and the North Atlantic Oscillation. *J. Climate*, **13**, 2550–2569, https://doi.org/10.1175/1520-0442(2000)013<2550:TRBDVO>2.0.CO;2.

——, Y.-O. Kwon, and L. Yu, 2009: On the relationship between synoptic wintertime atmospheric variability and path shifts in the Gulf Stream and the Kuroshio Extension. *J. Climate*, **22**, 3177–3192, https://doi.org/10.1175/2008JCLI2690.1.

——, ——, H. Seo, and C. C. Ummenhofer, 2019: Meridional Gulf Stream shifts can influence wintertime variability in the North Atlantic storm track and Greenland blocking. *Geophys. Res. Lett.*, **46**, 1702–1708, https://doi.org/10.1029/2018GL081087.

Kallberg, P., P. Berrisford, B. J. Hoskins, A. Simmons, S. Uppala, S. Lamy-Thepaut, and R. Hine, 2005: ERA-40 Atlas. ERA-40 Project Report Series, Vol. 19, ECMWF, 199 pp.

Kelly, K. A., and B. Qiu, 1995: Heat flux estimates for the western North Atlantic. Part II: The upper-ocean heat balance. *J. Phys. Oceanogr.*, **25**, 2361–2373, https://doi.org/10.1175/1520-0485(1995)025<2361:HFEFTW>2.0.CO;2.

——, R. J. Small, R. M. Samelson, B. Qiu, T. M. Joyce, Y.-O. Kwon, and M. F. Cronin, 2010: Western boundary currents and frontal air–sea interaction: Gulf Stream and Kuroshio Extension. *J. Climate*, **23**, 5644–5667, https://doi.org/10.1175/2010JCLI3346.1.

Kennedy, J., H. Titchner, N. Rayner, and M. Roberts, 2017: input4MIPs.MOHC.SSTsAndSeaIce.HighResMIP.MOHC-HadISST-2-2-0-0-0, version 20170505. Earth System Grid Federation, accessed 5 May 2017, https://doi.org/10.22033/ESGF/input4MIPs.1221.

Kushnir, Y., W. A. Robinson, I. Bladé, N. M. J. Hall, S. Peng, and R. Sutton, 2002: Atmospheric GCM response to extratropical SST anomalies: Synthesis and evaluation. *J. Climate*, **15**, 2233–2256, https://doi.org/10.1175/1520-0442(2002)015<2233:AGRTES>2.0.CO;2.

Kwon, Y.-O., and T. M. Joyce, 2013: Northern Hemisphere winter atmospheric transient eddy heat fluxes and the Gulf Stream and Kuroshio–Oyashio Extension variability. *J. Climate*, **26**, 9839–9859, https://doi.org/10.1175/JCLI-D-12-00647.1.

——, M. Alexander, N. Bond, C. Frankignoul, H. Nakamura, B. Qiu, and L. Thompson, 2010: Role of the Gulf Stream and Kuroshio–Oyashio systems in large-scale atmosphere–ocean interaction: A review. *J. Climate*, **23**, 3249–3281, https://doi.org/10.1175/2010JCLI3343.1.

Ma, X., P. Chang, R. Saravanan, R. Montuoro, H. Nakamura, D. Wu, X. Lin, and L. Wu, 2017: Importance of resolving Kuroshio front and eddy influence in simulating the North Pacific storm track. *J. Climate*, **30**, 1861–1880, https://doi.org/10.1175/JCLI-D-16-0154.1.

Madonna, E., C. Li, C. M. Grams, and T. Woollings, 2017: The link between eddy-driven jet variability and weather regimes in the North Atlantic–European sector. *Quart. J. Roy. Meteor. Soc.*, **143**, 2960–2972, https://doi.org/10.1002/qj.3155.

Minobe, S., A. Kuwano-Yoshida, N. Komori, S.-P. Xie, and R. J. Small, 2008: Influence of the Gulf Stream on the troposphere. *Nature*, **452**, 206–209, https://doi.org/10.1038/nature06690.

——, M. Miyashita, A. Kuwano-Yoshida, H. Tokinaga, and S.-P. Xie, 2010: Atmospheric response to the Gulf Stream: Seasonal variations. *J. Climate*, **23**, 3699–3719, https://doi.org/10.1175/2010JCLI3359.1.

Nakamura, H., T. Sampe, Y. Tanimoto, and A. Shimpo, 2004: Observed associations among storm tracks, jet streams and midlatitude oceanic fronts. *Earth's Climate: The Ocean–Atmosphere Interaction, Geophys. Monogr.*, Vol. 147, Amer. Geophys. Union, 329–345, https://doi.org/10.1029/147GM18.

Nakamura, M., and S. Yamane, 2009: Dominant anomaly patterns in the near-surface baroclinicity and accompanying anomalies in the atmosphere and oceans. Part I: North Atlantic basin. *J. Climate*, **22**, 880–904, https://doi.org/10.1175/2008JCLI2297.1.

——, and ——, 2010: Dominant anomaly patterns in the near-surface baroclinicity and accompanying anomalies in the atmosphere and oceans. Part II: North Pacific basin. *J. Climate*, **23**, 6445–6467, https://doi.org/10.1175/2010JCLI3017.1.

Novak, L., M. H. P. Ambaum, and R. Tailleux, 2015: The life cycle of the North Atlantic storm track. *J. Atmos. Sci.*, **72**, 821–833, https://doi.org/10.1175/JAS-D-14-0082.1.

O'Reilly, C. H., and A. Czaja, 2015: The response of the Pacific storm track and atmospheric circulation to Kuroshio Extension variability. *Quart. J. Roy. Meteor. Soc.*, **141**, 52–66, https://doi.org/10.1002/qj.2334.

——, S. Minobe, A. Kuwano-Yoshida, and T. Woollings, 2017: The Gulf Stream influence on wintertime North Atlantic jet variability. *Quart. J. Roy. Meteor. Soc.*, **143**, 173–183, https://doi.org/10.1002/qj.2907.

Orlanski, I., 2003: Bifurcation in eddy life cycles: Implications for storm track variability. *J. Atmos. Sci.*, **60**, 993–1023, https://doi.org/10.1175/1520-0469(2003)60<993:BIELCI>2.0.CO;2.

Palmer, T. N., 1993: A nonlinear dynamical perspective on climate change. *Weather*, **48**, 314–326, https://doi.org/10.1002/j.1477-8696.1993.tb05802.x.

Pan, J., X.-H. Yan, Q. Zheng, and W. T. Liu, 2002: Observation of western boundary current atmospheric convergence zones using scatterometer winds. *Geophys. Res. Lett.*, **29**, 1832, https://doi.org/10.1029/2002GL015015.

Parfitt, R., and H. Seo, 2018: A new framework for near-surface wind convergence over the Kuroshio extension and Gulf Stream in winter time: The role of atmospheric fronts. *Geophys. Res. Lett.*, **45**, 9909–9918, https://doi.org/10.1029/2018GL080135.

Patrizio, C. R., and D. W. Thompson, 2021: Quantifying the role of ocean dynamics in ocean mixed-layer temperature variability. *J. Climate*, **34**, 2567–2589, https://doi.org/10.1175/JCLI-D-20-0476.1.

Peng, S., and J. S. Whitaker, 1999: Mechanisms determining the atmospheric response to midlatitude SST anomalies. *J. Climate*, **12**, 1393–1408, https://doi.org/10.1175/1520-0442(1999)012<1393:MDTART>2.0.CO;2.

——, W. A. Robinson, and M. P. Hoerling, 1997: The modeled atmospheric response to midlatitude SST anomalies and its dependence on background circulation states. *J. Climate*, **10**, 971–987, https://doi.org/10.1175/1520-0442(1997)010<0971:TMARTM>2.0.CO;2.

Roberts, C. D., R. Senan, F. Molteni, S. Boussetta, M. Mayer, and S. P. E. Keeley, 2018: Climate model configurations of the ECMWF Integrated Forecasting System (ECMWF-IFS cycle 43R1) for HighResMIP. *Geosci. Model Dev.*, **11**, 3681–3712, https://doi.org/10.5194/gmd-11-3681-2018.

Roberts, M. J., and Coauthors, 2019: Description of the resolution hierarchy of the global coupled HadGEM3-GC3.1 model as used in CMIP6 HighResMIP experiments. *Geosci. Model Dev.*, **12**, 4999–5028, https://doi.org/10.5194/gmd-12-4999-2019.

Sanchez-Franks, A., S. Hameed, and R. E. Wilson, 2016: The Icelandic low as a predictor of the Gulf Stream north wall position. *J. Phys. Oceanogr.*, **46**, 817–826, https://doi.org/10.1175/JPO-D-14-0244.1.

Sato, K., J. Inoue, and M. Watanabe, 2014: Influence of the Gulf Stream on the Barents Sea ice retreat and Eurasian coldness during early winter. *Environ. Res. Lett.*, **9**, 084009, https://doi.org/10.1088/1748-9326/9/8/084009.

Sheldon, L., A. Czaja, B. Vannière, C. Morcrette, B. Sohet, M. Casado, and D. Smith, 2017: A 'warm path' for Gulf Stream–troposphere interactions. *Tellus*, **69A**, 1299397, https://doi.org/10.1080/16000870.2017.1299397.

Smirnov, D., M. Newman, and M. A. Alexander, 2014: Investigating the role of ocean–atmosphere coupling in the North Pacific Ocean. *J. Climate*, **27**, 592–606, https://doi.org/10.1175/JCLI-D-13-00123.1.

——, ——, ——, Y.-O. Kwon, and C. Frankignoul, 2015: Investigating the local atmospheric response to a realistic shift in the Oyashio sea surface temperature front. *J. Climate*, **28**, 1126–1147, https://doi.org/10.1175/JCLI-D-14-00285.1.

Stone, P. H., 1978: Baroclinic adjustment. *J. Atmos. Sci.*, **35**, 561–571, https://doi.org/10.1175/1520-0469(1978)035<0561:BA>2.0.CO;2.

Taylor, A. H., and J. A. Stephens, 1998: The North Atlantic Oscillation and the latitude of the Gulf Stream. *Tellus*, **50A**, 134–142, https://doi.org/10.3402/tellusa.v50i1.14517.

Vivier, F., K. A. Kelly, and L. A. Thompson, 2002: Heat budget in the Kuroshio Extension region: 1993–99. *J. Phys. Oceanogr.*, **32**, 3436–3454, https://doi.org/10.1175/1520-0485(2002)032<3436:HBITKE>2.0.CO;2.

Watanabe, M., and M. Kimoto, 2000: Atmosphere–ocean thermal coupling in the North Atlantic: A positive feedback. *Quart. J. Roy. Meteor. Soc.*, **126**, 3343–3369, https://doi.org/10.1002/qj.49712657017.

Willison, J., W. A. Robinson, and G. M. Lackmann, 2013: The importance of resolving mesoscale latent heating in the North Atlantic storm track. *J. Atmos. Sci.*, **70**, 2234–2250, https://doi.org/10.1175/JAS-D-12-0226.1.

Wills, S. M., D. W. J. Thompson, and L. M. Ciasto, 2016: On the observed relationships between variability in Gulf Stream sea surface temperatures and the atmospheric circulation over the North Atlantic. *J. Climate*, **29**, 3719–3730, https://doi.org/10.1175/JCLI-D-15-0820.1.

Woollings, T., and B. Hoskins, 2008: Simultaneous Atlantic–Pacific blocking and the northern annular mode. *Quart. J. Roy. Meteor. Soc.*, **134**, 1635–1646, https://doi.org/10.1002/qj.310.

——, A. Hannachi, and B. Hoskins, 2010: Variability of the North Atlantic eddy-driven jet stream. *Quart. J. Roy. Meteor. Soc.*, **136**, 856–868, https://doi.org/10.1002/qj.625.